A framework for modeling bioimpedance measurements of nonhomogeneous tissues: a theoretical and simulation study

Xuesong Luo[1,2], Shaoping Wang[1] and Benjamin Sanchez[2] ‡

[1]Department of Automation Science and Electric Engineering, Beijing Advanced Innovation Center for Big Data-Based Precision Medicine, Beihang University, Beijing 100083, China.
[2]Sanchez Research Lab, Department of Electrical and Computer Engineering, University of Utah, Salt Lake City, UT 84112-9206, USA.

E-mail: benjamin.sanchez@utah.edu

Abstract. *Objective*: Bioimpedance technology is experiencing an increased use to assess health in a wide range of new consumer, research and clinical applications. However, the interaction between tissues producing bioimpedance data is often unclear. *Methods*: This work provides a novel theoretical framework to model bioimpedance measurements of nonhomogeneous tissues. We consider five case studies to validate the usefulness of our approach against finite element model (FEM) simulations. *Results*: Theoretical and FEM-simulated apparent resistance and reactance data were in good agreement, with a maximum relative errors $< 4\%$ and $< 8\%$, respectively. *Conclusion*: The biophysics-driven framework developed provides compact analytical expressions to model nonhomogeneous bioimpedance measurements including multiple tissues with arbitrary shape and electrical properties. This work provides a new perspective to interpret nonhomogeneous bioimpedance measurements using *series*, *parallel*, and *series-parallel* circuit-like topology equivalents. *Significance*: Our framework is a new tool to better understand and describe complex nonhomogeneous biological measurements as, for example, cardiac, brain and respiratory applications using (non)invasive electrodes.

Keywords: electrical bioimpedance, nonhomogeneous tissue, finite element model, forward model.

‡ Corresponding author: Dr. Benjamin Sanchez, Sorenson Molecular Biotechnology Building, Office 3721, 36 South Wasatch Drive, University of Utah, Salt Lake City, UT 84112-9206, USA, phone: (801) 585-9535, email: benjamin.sanchez@utah.edu.

1. Introduction

Bioimpedance technology can detect cancerous lymph nodes (Hong et al. 2020), diagnose a broad range of disorders (Ibrahim et al. 2005, Haas et al. 2012, Cumming et al. 2014, Zamani et al. 2018, Parke et al. 2015, Rutkove & Sanchez 2018) and evaluate treatment outcomes (Lorenzo et al. 2020). The working principle consists of applying a nonstimulating, nonionizing electrical current through tissue using two dedicated current electrodes and recording the voltage generated with a second pair of dedicated electrodes. From the amplitude and time-lag relationship between the current and voltage signals, impedance data is measured (Grimnes & Martinsen 2011).

The impedance reflects the exogenous electrical conduction property of tissues. These electrical properties measure how strongly tissue resists (or conducts) alternating electric current and how capable is the tissue to store electric charge within itself (Schwan & Foster 1989). They are determined by the electrical properties, namely the conductivity σ (S m^{-1}) and the relative permittivity ε_r (dimensionless), relative to the permittivity of the vacuum ε_0 (F m^{-1}). In skeletal muscle for example, these two fundamental electrical properties change with disease progression (Sanchez et al. 2020).

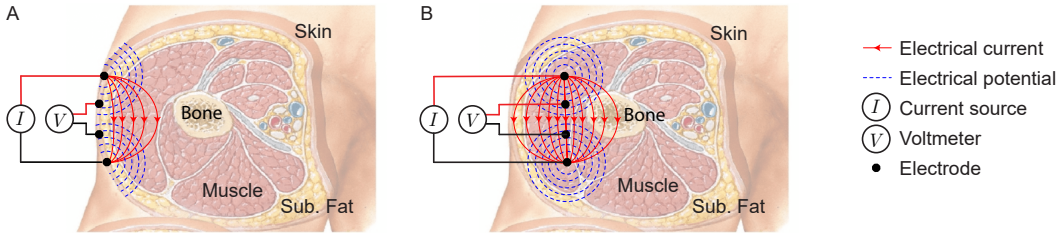

Figure 1. Illustration of tetrapolar bioimpedance measurement of nonhomogeneous tissue using surface (A) and penetrating (B) electrodes. In the schematic, the outer two electrodes are the high (source) and low (sink) current electrodes, whereas the inner electrodes are the high and low potential recording electrodes required for bioimpedance measurement.

As illustrated in Figure 1, the electrical current applied for the biompedance measurement might flow through more than one tissue or fluid, each with different electrical properties. Formally, these different tissues and fluids will contribute to the *apparent* impedance $Z \in \mathbb{C}$ (Ohms) measured as follows (Geselowitz 1971)

$$Z = \int_{\Omega} \left(\frac{\mathbf{J}^{I}(\mathbf{r})}{\sigma(\mathbf{r}) + \tau \omega_k \varepsilon_r(\mathbf{r}) \varepsilon_0} \right) \cdot \mathbf{J}^{V}(\mathbf{r}) \, d\mathbf{r},$$

where $\Omega \in \mathbb{R}^3$ is the domain with coordinate system $\mathbf{r} := (x, y, z)$, $\mathbf{J}^{I,V} \in \mathbb{C}$ (m^{-2}) are the local current density vectors found swapping the injection of electrical current between the current I and voltage V electrodes, respectively, $\omega_k \in \mathbb{R}$ (rad s^{-1}) is the (angular) frequency of electrical current, and $\tau := \sqrt{-1}$ is the imaginary unit (dimensionless). The above expression shows that depending on (1) the electrodes, (2) the domain and (3) the electrical properties of the tissues

within the domain, the apparent impedance might represent an amalgam of different tissues. For example, in a localized surface electrical impedance myography measurements, data are influenced by skin and subcutaneous fat tissues at the recording site (Kwon, Malik, Rutkove & Sanchez 2019). If the electrodes are placed farther apart on a limb for example, then the impedance will become dependent on the geometry of the domain (Bachasson et al. 2021). Figure 2 summarizes the complexity of the different existing bioimpedance models according to the electrodes, domain and tissue.

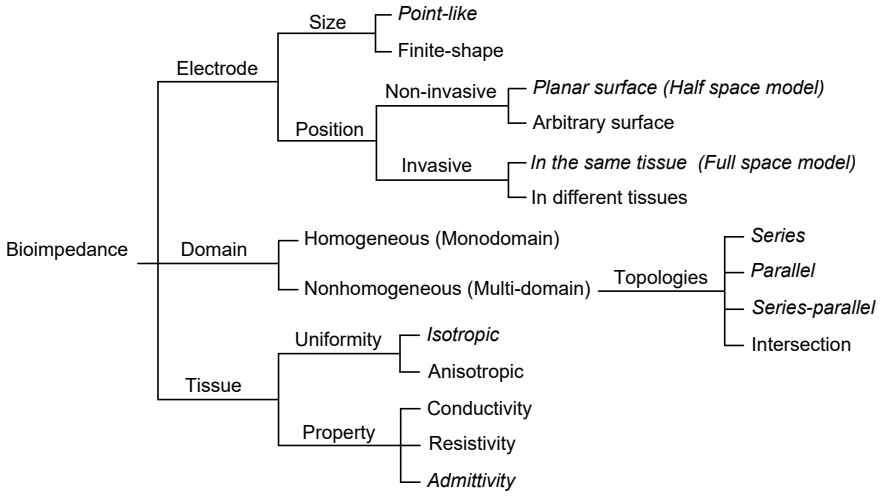

Figure 2. Summary of forward bioimpedance models. The assumptions of the framework developed in this study are italicized.

In this paper we develop a framework capable of describing nonhomogeneous impedance measurement containing multiple tissues with different electrical properties, electrodes' positioning, and arbitrary domain shapes. The paper is organized as follows. We first define a nonhomogeneous model using mathematical notation in Section 2. Then nonhomogeneous impedance of *series*, *parallel*, *series-parallel* circuit-like topologies are analytically modeled in half space in Section 3, 4, 5, respectively. Section 6 extends the *series-parallel* circuit-like topology model to full space. Section 7 describes the simulation settings and the simulation results in Section 8 confirm the usefulness of the novel framework presented. Finally, the contribution is discussed in Section 9 and summarized in the form of conclusions in Section 10.

2. Nonhomogeneous tissues: *series*, *parallel*, and *series-parallel* circuit-like topologies

In this paper we model nonhomogeneous tissue as a semi-infinite space $\Lambda_- \in \mathbb{R}^3_-$ and infinite space $\Lambda \in \mathbb{R}^3$ containing $M \in \mathbb{N}_{\geq 1}$ domains. Then, we study bioimpedance measurements in $\{\Lambda_-, \Lambda\}$ considering 3 different nonhomogeneous "electrical circuit-like" topologies shown in Figure 3 according to how the current flows from one domain to another: *series*, *parallel* and *series-parallel*, formally defined next. Let's start by considering M *non-overlapping* domains $\Omega_i \in \{\Lambda_-, \Lambda\}$ with $i \in \{1, 2, \cdots, M\}$, where each domain has different electrical properties

(these electrical properties are defined in the next section) satisfying $\bigcup_{1\leq i\leq M}\Omega_i = \{\Lambda_-, \Lambda\}$. We next define $\partial\Omega_i$ as the outer surface boundary of Ω_i. Then, $\forall i, j \in \{1, 2, \cdots, M\}$ and $i \neq j$, two domains are non-overlapping if $\Omega_i \cap \Omega_j = \partial\Omega_k$ where $k \in \{i, j\}$ or $\Omega_i \cap \Omega_j = \varnothing$. Note that in the case where $\Omega_i \cap \Omega_j = \partial\Omega_k$, the electrical current can propagate from Ω_i to Ω_j through the boundary Ω_k directly, whereas in the case where $\Omega_i \cap \Omega_j = \varnothing$ the current must propagate through another domain first.

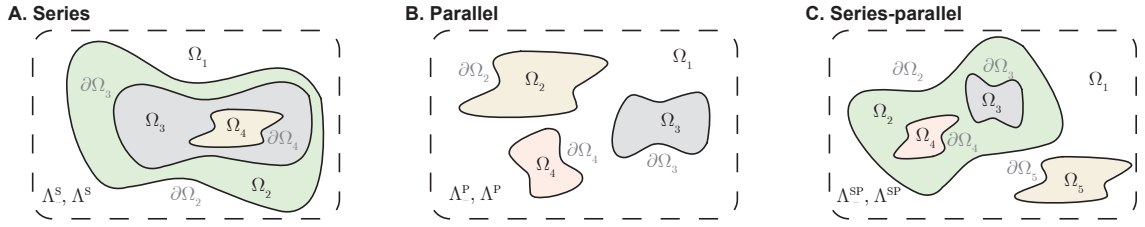

Figure 3. Schematic representing nonhomogeneous tissue as a semi-infinite domain $\Lambda_- \in \mathbb{R}^3_-$ and infinite domain $\Lambda \in \mathbb{R}^3$ with (A) *series* (denoted by the superscript S), (B) *parallel* (denoted by the superscript P) and (C) *series-parallel* (denoted by the superscript SP) electrical circuit-like topology containing $M = 5$ subdomains Ω_i with boundary $\partial\Omega_i$ and $i \in \{1, \cdots, M\}$.

We define Ω_i neighbor to Ω_j as $i|j$ when $\Omega_i \cap \Omega_j = \partial\Omega_k$. The neighbor definition satisfies the principle of reciprocity, that is to say, Ω_i is neighbor to Ω_j, and vice versa. Then, we can define a neighbor set $N(\Omega_i) := \{\Omega_j | (i|j)\}$ for domain Ω_i as the set containing all neighbors of Ω_i. Moreover, we define the cardinality of neighbor set $|N(\Omega_i)|$ as the number of all elements in $N(\Omega_i)$. Henceforth, superscripts $+$ and $-$ of $N(\Omega_i)$ refer to the neighbors *outside* and *inside* Ω_i, respectively, so that $|N(\Omega_i)| = |N^+(\Omega_i)| + |N^-(\Omega_i)|$. To describe the elements in $N^\pm(\Omega_i)$, we use the notation $i^\pm \in \{j | \Omega_j \in N^\pm(\Omega_i)\}$. Then, the outer/inner neighbor relation of Ω_i is $\Omega_{i^\pm} \in N^\pm(\Omega_i)$. Finally, using these notations, we can define *series*, *parallel* and *series-parallel* topology as shown in Table 3. Note that series and parallel topology are two specific cases of a more general series-parallel topology.

Next we develop in Sections 3, 4 and 5 a forward analytical framework modeling tetrapolar impedance measurements of nonhomogeneous tissue considering a series, parallel and series-parallel circuit-like topologies, respectively.

3. Electrical impedance model in half space with *series* circuit-like topology

The coordinate $\mathbf{r} := (x, y, z)$ defines a position in Λ^{S}_-, where the superscript S denotes a *series* circuit-like topology. To determine the electrical potential distribution within Λ^{S}_- (see Figure 4 A), we consider a sinusoidal electrical current of amplitude $I \in \mathbb{R}$ at (angular) frequency $\omega_k \in \mathbb{R}_{>0}$ (rad s^{-1}), generated by point-like source S at $\mathbf{r}_{\mathrm{S}} := (x_{\mathrm{S}}, y_{\mathrm{S}}, 0)$ with current sink at infinity. In other words, this assumption reduces to considering only one (positive) current being applied to the model responsible of generating the distribution of electrical potential. The voltage recording point-like electrode E at $\mathbf{r}_{\mathrm{E}} := (x_{\mathrm{E}}, y_{\mathrm{E}}, 0)$ is then placed on $\partial\Omega_1 : z = 0$ to record the electrical potential with reference zero potential at infinity. Henceforth, we have following assumptions: (1) the current source and voltage recording electrodes are

Table 1. Definitions of *series*, *parallel*, *series-parallel* circuit-like topology for nonhomogeneous tissue with $i, i^{\pm} \in \{1,2,3,\cdots,M\}$.

Topology	Definition	Property
Series	$\lvert N(\Omega_1)\rvert = \lvert N^-(\Omega_1)\rvert = 1$, $\lvert N^+(\Omega_i)\rvert = \lvert N^-(\Omega_i)\rvert = 1$, and $\lvert N(\Omega_M)\rvert = \lvert N^+(\Omega_M)\rvert = 1$, where $i \neq 1, M$	$\Omega_i \in N^-(\Omega_{i-1})$ where $i \neq 1$
Parallel	$\lvert N(\Omega_1)\rvert = \lvert N^-(\Omega_1)\rvert = M-1$ and $\lvert N(\Omega_i)\rvert = \lvert N^+(\Omega_i)\rvert = 1$, where $i \neq 1$	$\Omega_i \in N^-(\Omega_1)$ where $i \neq 1$
Series-parallel	$\lvert N^+(\Omega_1)\rvert = 0$, $\lvert N^+(\Omega_i)\rvert = 1$, and $\lvert N(\Omega_M)\rvert = \lvert N^+(\Omega_M)\rvert = 1$, where $i \neq 1, M$.	$\Omega_{i^+} \in N^+(\Omega_i)$ and $\Omega_{i^-} \in N^-(\Omega_i)$

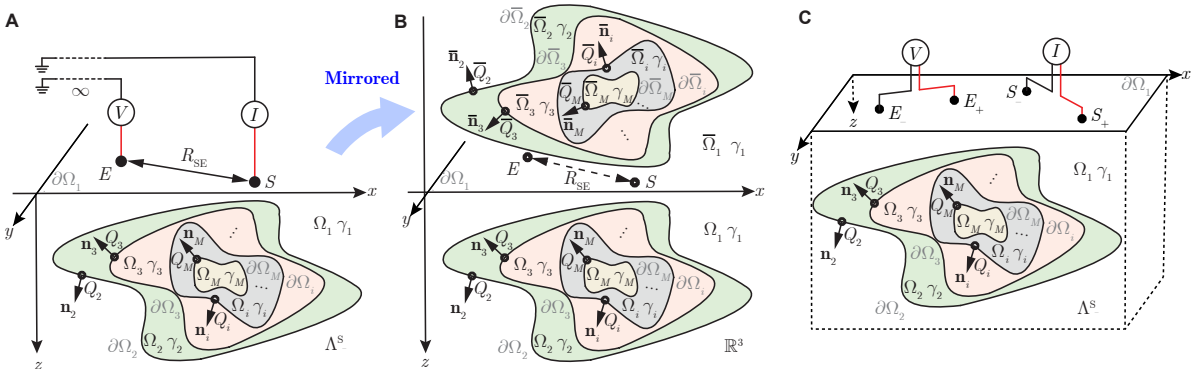

Figure 4. (A) Schematic illustrating a nonhomogeneous tissue modeled as *series* circuit-like topology in half space Λ^S_- (A) and its mirrored image in $\mathbb{R}^3$ (B). There are M nested domains Ω_i in Λ^S_- where $i \in \{1,2,3,\cdots,M\}$. Surface $\partial\Omega_i$ is the outer boundary of Ω_i with isotropic admittivity is γ_i. Surface $\partial\Omega_1$ is a plane $(x,y,0)$ while other surface $\partial\Omega_i$ $(i \neq 1)$ have arbitrary surfaces. A point source S at $\mathbf{r}_S := (x_S, y_S, 0)$ on $\partial\Omega_1$ generates sinusoidal current. Another point E at $\mathbf{r}_E := (x_E, y_E, 0)$ is a potential recording electrode on $\partial\Omega_1$. Point Q_i $(i > 1)$ is at position $\mathbf{r}_{Q_i} := (x_{Q_i}, y_{Q_i}, z_{Q_i})$ on $\partial\Omega_i$, and $\mathbf{n}_i$ is the outward normal vector of $\partial\Omega_i$ at Q_i. R_{SE} is the distance between S and E. (B) The half-space model Λ^S_- is mirrored with respect to plane $\partial\Omega_1$ and forms the mirrored full space $\mathbb{R}^3$. All mirrored elements in (B) are overlined to distinguish form their nonmirrored counterparts shown in (A). (C) Schematic illustrating a tetrapolar electrical impedance measurement on $\partial\Omega_1$ for Λ^S_-. The current source $(+)$ and sink $(-)$ electrodes are $S_\pm$ and the high $(+)$ and low $(-)$ voltage measuring electrodes are $E_\pm$ placed on $\partial\Omega_1$.

dimensionless; (2), the domains have isotropic electrical properties; (3), there are no free charges in the model; and (4), the current cannot flow outside the model.

3.1. Governing equation

From Maxwell equations in quasistationary regime (Maxwell 1873), the governing equation of the electrical potential distribution $U^{\mathrm{S}}(\mathbf{r}) \in \mathbb{C}$ (V) is the generalized Poisson equation

$$\nabla \cdot \Big(\gamma^{\mathrm{S}}(\mathbf{r}) \nabla U^{\mathrm{S}}(\mathbf{r}) \Big) = -I\delta(\mathbf{r} - \mathbf{r}_{\mathrm{S}}), \tag{1}$$

where $\gamma^{\mathrm{S}} \in \mathbb{C}$ (S m^{-1}) is the nonhomogeneous admittivity property and $\delta(\mathbf{r})$ is the Dirac delta function. To solve (1), we first need to describe the admittivity distribution in Λ^{S}_{-}. The isotropic admittivity in domain Ω_i is defined as $\gamma_i := \sigma_i + \tau\omega_k\varepsilon_i$, $\sigma_i \in \mathbb{R}_{>0}$ and $\varepsilon_i \in \mathbb{R}_{>0}$ are the conductivity (S m^{-1}) and the absolute permittivity (F m^{-1}) properties in Ω_i at frequency ω_k, respectively. Due to the nested structure of subdomains in Λ^{S}_{-} shown in Figure 4 A, the admittivity distribution $\gamma^{\mathrm{S}}(\mathbf{r})$ can be explicitly described from series topology in Table 3 as

$$\gamma^{\mathrm{S}}(\mathbf{r}) := \gamma_1 + \sum_{i=2}^{M} (\gamma_i - \gamma_{i-1}) H(\mathbf{r} + \mathbf{n}_i), \tag{2}$$

where function $H(\mathbf{r})$ is the Heaviside unit step function, vector $\mathbf{n}_i$ is the outward normal vector of $\partial\Omega_i$ at point Q_i, the latter an arbitrary point on $\partial\Omega_i$. Applying the half-maximum convention of $H(\mathbf{r})$, one can find admittivity $(\gamma_i + \gamma_{i-1})/2$ on $\partial\Omega_i$ with $i \neq 1$ from (2). Then, the Dirac delta function $\delta(\mathbf{r})$ can be expressed as the divergence of Heaviside unit step function $\nabla H(\mathbf{r}_{\mathrm{Q}_i}) = \delta(\mathbf{r}_{\mathrm{Q}_i})\mathbf{n}_i$, where $\mathbf{r}_{\mathrm{Q}_i} := (x_{\mathrm{Q}_i}, y_{\mathrm{Q}_i}, z_{\mathrm{Q}_i})$ is the position at Q_i. Then we can rewrite (1) as

$$\nabla^2 U^{\mathrm{S}}(\mathbf{r}) = -\frac{I\delta(\mathbf{r} - \mathbf{r}_{\mathrm{S}})}{\gamma^{\mathrm{S}}(\mathbf{r})} - 2\sum_{i=2}^{M} \Gamma_{i-1|i}\delta(\partial\Omega_i) \frac{\partial U^{\mathrm{S}}(\mathbf{r})}{\partial \mathbf{n}_i} \cdot \mathbf{n}_i, \tag{3}$$

where $\mathbf{r} \neq \mathbf{r}_{\mathrm{S}}$, $\Gamma_{i|j} \in \mathbb{C}$ (dimensionless) is the reflection coefficient of the boundary between subdomains Ω_i and Ω_j defined as $\Gamma_{i|j} := (\gamma_i - \gamma_j)/(\gamma_i + \gamma_j)$ with $i, j \in \{1, 2, \cdots, M\}$ and $i \neq j$.

The boundary condition is $\partial U^{\mathrm{S}}(\mathbf{r})/\partial z\big|_{\partial\Omega_1} = 0$. To satisfy this boundary condition, we apply the method of images charges to (3). As shown in Figure 4 B, the half space model Λ^{S}_{-} is mirrored with respect to the plane $z = 0$ to construct a full space model in $\mathbb{R}^3$. Considering the image reflection term, the governing equation becomes

$$\nabla^2 U^{\mathrm{S}}(\mathbf{r}) = -\frac{2I\delta(\mathbf{r} - \mathbf{r}_{\mathrm{S}})}{\gamma^{\mathrm{S}}(\mathbf{r})} - 2\sum_{i=2}^{M} \Gamma_{i-1|i} \left[\delta(\partial\Omega_i) \frac{\partial U^{\mathrm{S}}(\mathbf{r})}{\partial \mathbf{n}_i} \cdot \mathbf{n}_i + \delta(\partial\overline{\Omega}_i) \frac{\partial U^{\mathrm{S}}(\mathbf{r})}{\partial \overline{\mathbf{n}}_i} \cdot \overline{\mathbf{n}}_i \right], \tag{4}$$

where all overlined notations are mirrored elements from their original counterparts with respect to the plane $\partial\Omega_1$.

3.2. Electrical potential distribution

To obtain the expression of potential $U^{\mathrm{S}}(\mathbf{r})$ analytically, we simplify (4) with the method of Green's function as in (Cohl & Tohline 1999), namely

$$\begin{cases} U^{\mathrm{S}}(\mathbf{r}) & = U_0(\mathbf{r}) + \sum_{i=2}^{M} U_{\Omega_i}^{\mathrm{S}}(\mathbf{r}) \\ U_0(\mathbf{r}) & = \frac{I}{2\pi\gamma_1 |\mathbf{r}-\mathbf{r}_{\mathrm{S}}|} \\ U_{\Omega_i}^{\mathrm{S}}(\mathbf{r}) & = \frac{\Gamma_{i-1|i}}{2\pi} \left[\iint_{\partial\Omega_i} \frac{\partial U^{\mathrm{S}}(\mathbf{r}_{\mathrm{Q}_i})}{\partial \mathbf{n}_i} \cdot \mathbf{n}_i \frac{\mathrm{d}(\partial\Omega_i)}{\left|\mathbf{r}-\mathbf{r}_{\mathrm{Q}_i}\right|} + \iint_{\partial\overline{\Omega}_i} \frac{\partial U^{\mathrm{S}}(\mathbf{r}_{\overline{\mathrm{Q}}_i})}{\partial \overline{\mathbf{n}}_i} \cdot \overline{\mathbf{n}}_i \frac{\mathrm{d}\left(\partial\overline{\Omega}_i\right)}{\left|\mathbf{r}-\mathbf{r}_{\overline{\mathrm{Q}}_i}\right|} \right], \end{cases} \tag{5}$$

where operator $|\cdot|$ is the L_2 norm, $\mathrm{d}\left(\partial\Omega_i\right)$ and $\mathrm{d}\left(\partial\overline{\Omega}_i\right)$ represent the area of the micro-elements $\partial\Omega_i$ and $\partial\overline{\Omega}_i$ at Q_i and $\overline{\mathrm{Q}}_i$, respectively. We next solve (5) using an iterative approximation. Following the same rationale as in (Wazwaz 2007), the pth-order approximated (denoted by $\widetilde{\ }$) electrical potential distribution with series topology $\widetilde{U}^{\mathrm{S}(p)}(\mathbf{r}) \in \mathbb{C}$ (V) is defined as

$$\begin{cases} \widetilde{U}^{\mathrm{S}(p)}(\mathbf{r}) & := U_0(\mathbf{r}) + \sum_{i=2}^{M} \widetilde{U}_{\Omega_i}^{\mathrm{S}(p)}(\mathbf{r}) \\ \widetilde{U}^{\mathrm{S}(0)}(\mathbf{r}) & := U_0(\mathbf{r}) \\ \widetilde{U}_{\Omega_i}^{\mathrm{S}(p)}(\mathbf{r}) & := \frac{\Gamma_{i-1|i}}{2\pi} \left[\iint_{\partial\Omega_i} \frac{\partial \widetilde{U}^{\mathrm{S}(p-1)}(\mathbf{r}_{\mathrm{Q}_i})}{\partial \mathbf{n}_i} \cdot \mathbf{n}_i \frac{\mathrm{d}(\partial\Omega_i)}{\left|\mathbf{r}-\mathbf{r}_{\mathrm{Q}_i}\right|} + \iint_{\partial\overline{\Omega}_i} \frac{\partial \widetilde{U}^{\mathrm{S}(p-1)}(\mathbf{r}_{\overline{\mathrm{Q}}_i})}{\partial \overline{\mathbf{n}}_i} \cdot \overline{\mathbf{n}}_i \frac{\mathrm{d}\left(\partial\overline{\Omega}_i\right)}{\left|\mathbf{r}-\mathbf{r}_{\overline{\mathrm{Q}}_i}\right|} \right], \end{cases} \tag{6}$$

where $p \in \mathbb{N}_{>0}$ is the order of approximation. According to the definition of reflection coefficient, we have $\left|\Gamma_{i|j}\right| \leq 1$. Then the analytical expression of potential distribution gives $U^{\mathrm{S}}(\mathbf{r}) = \lim_{p\to\infty} \widetilde{U}^{\mathrm{S}(p)}(\mathbf{r})$.

The electrical potential is recorded with electrode E at $\mathbf{r}_{\mathrm{E}} := (x_{\mathrm{E}}, y_{\mathrm{E}}, 0)$ (see Figure 4 A). Then, we can simplify the third expression in (6) based on the symmetry of image charges (see Figure 4 B) as

$$\widetilde{U}_{\Omega_i}^{\mathrm{S}(p)}(\mathbf{r}_{\mathrm{E}}) = \frac{\Gamma_{i-1|i}}{\pi} \iint_{\partial\Omega_i} \frac{\partial \widetilde{U}^{\mathrm{S}(p-1)}(\mathbf{r}_{\mathrm{Q}_i})}{\partial \mathbf{n}_i} \cdot \mathbf{n}_i \frac{\mathrm{d}\left(\partial\Omega_i\right)}{\left|\mathbf{r}_{\mathrm{E}} - \mathbf{r}_{\mathrm{Q}_i}\right|}.$$

The 1st-order approximated electrical potential can be deduced from (6) as

$$\widetilde{U}^{\mathrm{S}(1)}(\mathbf{r}_{\mathrm{E}}) = \frac{I}{2\pi\gamma_1} \left(\frac{1}{R_{\mathrm{SE}}} + 2 \sum_{i=2}^{M} K_{\Omega_i} \Gamma_{i-1|i} \right), \tag{7}$$

where

$$K_{\Omega_i} := -\frac{1}{2\pi} \iint_{\partial\Omega_i} \frac{\partial\left(\left|\mathbf{r}_{\mathrm{Q}_i} - \mathbf{r}_{\mathrm{S}}\right|\right)}{\partial \mathbf{n}_i} \cdot \mathbf{n}_i \frac{\mathrm{d}\left(\partial\Omega_i\right)}{\left|\mathbf{r}_{\mathrm{Q}_i} - \mathbf{r}_{\mathrm{S}}\right|^2 \left|\mathbf{r}_{\mathrm{E}} - \mathbf{r}_{\mathrm{Q}_i}\right|}$$

is a geometrical constant (m^{-1}) determined by the shape and position of Ω_i, and distance R_{SE} (m) between electrode S and E.

3.3. Apparent electrical impedance

Consider the tetrapolar impedance model shown in Figure 4 C where S_+ and S_- are the current source (+) and sink (−) electrodes (i.e., the potential generated by both the source and sink current electrodes), respectively, and where E_+ and E_- are the high (+) and low (−) voltage recording electrodes, respectively. The 1st-order potential difference $\Delta\widetilde{U}^{\mathrm{S}(1)} \in \mathbb{C}$ (V) is defined from (7) as

$$\Delta\widetilde{U}^{\mathrm{S}(1)} := \left(\widetilde{U}^{\mathrm{S}(1)}_{++} - \widetilde{U}^{\mathrm{S}(1)}_{+-}\right) - \left(\widetilde{U}^{\mathrm{S}(1)}_{-+} - \widetilde{U}^{\mathrm{S}(1)}_{--}\right),$$

where $\widetilde{U}^{\mathrm{S}(1)}_{++}$ and $\widetilde{U}^{\mathrm{S}(1)}_{+-}$ are the 1st-order approximation of the electrical potential generated by current source electrode S_+ and recorded by the high potential E_+ and low potential E_- electrode, respectively, $\widetilde{U}^{\mathrm{S}(1)}_{-+}$ and $\widetilde{U}^{\mathrm{S}(1)}_{--}$ are the first order approximation of the electrical potential generated by current source electrode S_- and recorded by the high potential E_+ and low potential E_- electrode, respectively. According to (7), we have

$$\Delta\widetilde{U}^{\mathrm{S}(1)} = \frac{I}{2\pi\gamma_1}\left(G + 2\sum_{i=2}^{M} K_i\Gamma_{i-1|i}\right) \tag{8}$$

where the geometrical constant $G := 1/R_{++} - 1/R_{+-} + 1/R_{--} - 1/R_{-+}$ (m^{-1}) is determined by the position of the current and voltage electrodes, R_{wv} (m) is the distance between electrode S_v and E_w with $w, v \in \{+,-\}$, the geometrical coefficient $K_i := K^{++}_{\Omega_i} - K^{+-}_{\Omega_i} + K^{--}_{\Omega_i} - K^{-+}_{\Omega_i}$ (m^{-1}) is determined by the shape and position of domain Ω_i with

$$K^{wv}_{\Omega_i} := -\frac{1}{2\pi}\iint_{\partial\Omega_i} \frac{\partial R_{\mathrm{Q}_i\mathrm{S}_v}(\mathbf{r}_{\mathrm{Q}_i})}{\partial \mathbf{n}_i}\cdot\mathbf{n}_i \frac{\mathrm{d}\left(\partial\Omega_i\right)}{R^2_{\mathrm{Q}_i\mathrm{S}_v}(\mathbf{r}_{\mathrm{Q}_i}) R_{\mathrm{Q}_i\mathrm{E}_w}(\mathbf{r}_{\mathrm{Q}_i})} \ (\mathrm{m}^{-1}),$$

where $R_{\mathrm{Q}_i\mathrm{S}_v}$ and $R_{\mathrm{Q}_i\mathrm{E}_w}$ (m) are the distance between point Q_i and electrodes S_v and E_w, respectively. From (8), the 1st-order approximated apparent electrical impedance $Z^{\mathrm{S}(1)} \in \mathbb{C}$ (Ohm) is expressed as

$$Z^{\mathrm{S}(1)} := R^{\mathrm{S}(1)} + \tau X^{\mathrm{S}(1)} = \frac{\Delta\widetilde{U}^{\mathrm{S}(1)}}{I} = \frac{1}{2\pi\gamma_1}\left(G + 2\sum_{i=2}^{M} K_i\Gamma_{i-1|i}\right), \tag{9}$$

where $R^{\mathrm{S}(1)}, X^{\mathrm{S}(1)} \in \mathbb{R}$ (Ohm) are the 1st-order approximated apparent resistance and reactance, respectively.

3.4. Apparent electrical impedance sensitivity to changes in tissue electrical properties

Next, we study the apparent impedance sensitivity to changes in intrinsic electrical properties within the model. For this, we define $\Delta\gamma_i := \Delta\sigma_i + \tau\omega\Delta\varepsilon_i$ in (9) and $|\Delta\gamma_i| \ll |\gamma_i|$. Then based on 1st-order Taylor series for $\Delta\gamma_i/\gamma_i$ in (9), one can approximate the apparent electrical

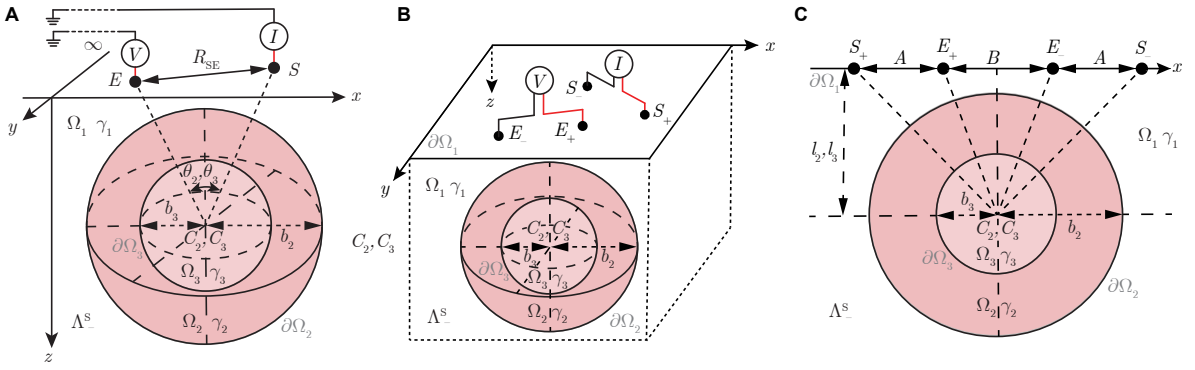

Figure 5. Schematic of case study 1. (A) Nonhomogeneous model $\Lambda^{\mathrm{S}}_{-} \in \mathbb{R}^3_-$ with *series* circuit-like topology consisting of a concentric spherical shell Ω_2 and kernel Ω_3 inside tissue Ω_1. The admittivity and outer boundary of Ω_i are γ_i and $\partial\Omega_i$, $i \in \{1,2,3\}$, with $\partial\Omega_1 := (x,y,0)$. Domains $\Omega_{\{2,3\}}$ are concentric at $C_{\{2,3\}}$ and radii $b_{\{2,3\}}$. A point-like source S at $\mathbf{r}_{\mathrm{S}} := (x_{\mathrm{S}}, y_{\mathrm{S}}, 0)$ generates electrical current. The point-like electrode E at $\mathbf{r}_{\mathrm{E}} := (x_{\mathrm{E}}, y_{\mathrm{E}}, 0)$ measures the electrical potential. Length R_{SE} is the distance between S and E. Angle θ is the angle between the line segment $|SC|$ and $|EC|$. (B) Schematic illustrating a surface tetrapolar electrical impedance measurement. The current source $(+)$ and sink $(-)$ electrodes are $S_\pm$ and the high $(+)$ and low $(-)$ voltage measuring electrodes are $E_\pm$ placed on $\partial\Omega_1$. (C) Tetrapolar electrical impedance measurement with linearly aligned current electrodes $S_\pm$ and measuring voltage electrodes $E_\pm$. The spherical center C satisfies $|CS_+| = |CS_-|$. The distance from $C_{\{2,3\}}$ to line segment $|E_+E_-|$ are $l_{\{2,3\}}$. The distances between current and voltage electrodes is A, whereas the distance between voltage electrodes is B.

impedance sensitivity $\Delta Z^{\mathrm{S}(1)}/Z^{\mathrm{S}(1)}$ to relative change of admittivity $\Delta\gamma_i/\gamma_i$, as follows

$$\frac{\Delta Z^{\mathrm{S}(1)}}{Z^{\mathrm{S}(1)}} \approx \begin{cases} -\frac{\Delta\gamma_i}{\gamma_i}\left(1 - \frac{2\varpi_{i|i+1}}{Z^{\mathrm{S}(1)}}\right) & \text{if} \quad i = 1 \\ -\frac{\Delta\gamma_i}{\gamma_i}\frac{2\varpi_{i-1|i}}{Z^{\mathrm{S}(1)}} & \text{if} \quad i = M \\ -\frac{\Delta\gamma_i}{\gamma_i}\left(\frac{2\varpi_{i-1|i}}{Z^{\mathrm{S}(1)}} + \frac{2\varpi_{i|i+1}}{Z^{\mathrm{S}(1)}}\right) & \text{else,} \end{cases} \tag{10}$$

where $\varpi_{j|i} := K_i\gamma_i\gamma_j/\left(\pi\gamma_1(\gamma_i+\gamma_j)^2\right)$ (Ohm).

3.5. Case study 1

Here we consider the case study of a nonhomogeneous tissue consisting of $M = 3$ domains where Ω_2 and Ω_3 are modeled as a concentric spherical shell-kernel (see Figure 5 A). The 1st-order approximated electrical potential distribution $\widetilde{U}^{\mathrm{S}(1)}(\mathbf{r}_{\mathrm{E}})$ recorded on $\partial\Omega_1$ can be expressed using (7) as follows

$$K_{\Omega_i} = \frac{1}{b_i}\sum_{n=0}^{\infty}\frac{2n}{2n+1}\left(\frac{b_i^2}{R_{\mathrm{SC}_i}R_{\mathrm{EC}_i}}\right)^{n+1} P_n(\cos\theta_i), \tag{11}$$

where $i \in \{2,3\}$, θ_i (rad) is the angle between line segment $|SC_i|$ and the line segment $|EC_i|$, $\cos\theta_i = (R^2_{\mathrm{SC}_i} + R^2_{\mathrm{EC}_i} - R^2_{\mathrm{SE}})/(2R_{\mathrm{SC}_i}R_{\mathrm{EC}_i})$, b_i (m) is the radius of Ω_i, R_{PC_i} (m) is the distance

between point $P \in \{S,E\}$ and C_i, and $P_n(x)$ are Legendre polynomials. We refer the reader to Lemma 1 in the Supplementary Information for further details regarding the mathematical derivation of the spherical geometrical coefficient in (11).

Figure 5 B illustrates the placement of current $S_\pm$ and voltage $E_\pm$ electrodes for impedance measurement. Then, the 1st-order approximated electrical potential difference, apparent electrical impedance and apparent impedance sensitivity can be evaluated using (8), (9) and (10), respectively, with

$$K_i = \sum_{n=0}^{\infty} G_{i,n}, \tag{12}$$

and

$$G_{i,n} := \frac{2nb_i^{2n+1}}{2n+1}\left(\frac{P_n(\cos\theta_{i++})}{R_{\mathrm{C}_i\mathrm{S}_+}^{n+1}R_{\mathrm{C}_i\mathrm{E}_+}^{n+1}} - \frac{P_n(\cos\theta_{i+-})}{R_{\mathrm{C}_i\mathrm{S}_-}^{n+1}R_{\mathrm{C}_i\mathrm{E}_+}^{n+1}} + \frac{P_n(\cos\theta_{i--})}{R_{\mathrm{C}_i\mathrm{S}_-}^{n+1}R_{\mathrm{C}_i\mathrm{E}_-}^{n+1}} - \frac{P_n(\cos\theta_{i-+})}{R_{\mathrm{C}_i\mathrm{S}_+}^{n+1}R_{\mathrm{C}_i\mathrm{E}_-}^{n+1}}\right),$$

in which θ_{ivw} (rad) with $w,v \in \{+,-\}$ is the angle between line segment $|C_iS_v|$ and $|C_iE_w|$, $R_{\mathrm{C}_i\mathrm{S}_v}$ and $R_{\mathrm{C}_i\mathrm{E}_w}$ (m) are the distances between C_i and S_v and E_w, respectively.

If we consider the electrodes are linearly aligned on $\partial\Omega_1$ and satisfy $|C_iS_+| = |C_iS_-|$ as illustrated in Figure 5 C, then we can simplify geometrical constant G in (8) and (9) as follows

$$G = \frac{2B}{A(A+B)}, \tag{13}$$

where A and B (m) are the interelectrode distances between current-voltage and voltage-voltage electrodes, respectively. We can also simplify $G_{i,n}$ in (12) as

$$G_{i,n} = \frac{4nb_i^{2n+1}}{2n+1}\left(\frac{4}{L_i}\right)^{n+1}\left(P_n\left(\frac{4l_i^2+t}{L_i}\right) - P_n\left(\frac{4l_i^2-t}{L_i}\right)\right)$$

and $G_{i,0} = 0$, where $L_i := \sqrt{(2A+B)^2+4l_i^2}\sqrt{B^2+4l_i^2}$ and $t := 2AB+B^2$, l_i is the distance (m) between C_i and the center of line segment $|E_+E_-|$.

3.6. Case study 2

Here we consider the case study of a nonhomogeneous layered tissue consisting of $M = 3$ domains and where Ω_1, Ω_2 and Ω_3 are stacked (see Figure 6 A). The model is defined by $\Omega_1 : 0 < z < h_1$, $\Omega_2 : h_1 < z < h_1 + h_2$ and $\Omega_3 : z > h_1 + h_2$ with planar boundaries $\partial\Omega_1 := (x,y,0)$, $\partial\Omega_2 := (x,y,h_1)$ and $\partial\Omega_3 := (x,y,h_2)$, respectively. Distances h_1 and h_2 (m) represent the thickness of tissues Ω_1 and Ω_2, respectively. The 1st-order approximated electrical potential distribution $\widetilde{U}^{\mathrm{S}(1)}(\mathbf{r}_\mathrm{E})$ on $\partial\Omega_1$ can be expressed using (7), where

$$K_{\Omega_i} = \frac{1}{\sqrt{R_{\mathrm{SE}}^2+4N_i^2}}, \tag{14}$$

where $i \in \{2,3\}$, $N_i := \sum_{j=1}^{i-1} h_j$ (m) is the distance from $\partial\Omega_i$ to $\partial\Omega_1$ and R_{SE} (m) is the distance between S and E. We refer the reader to Lemma 2 in the Supplementary Information

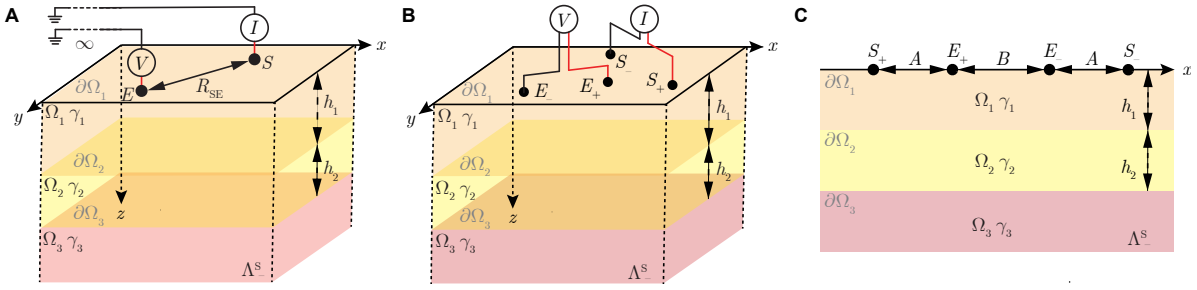

Figure 6. Schematic of case study 2. (A) Nonhomogeneous model $\Lambda^{\mathrm{S}}_{-} \in \mathbb{R}^3_{-}$ with *series* circuit-like topology consisting of a three-layered domain Ω_i, $i \in \{1,2,3\}$. The admittivity and boundary of domain Ω_i are γ_i and $\partial\Omega_1 := (x,y,0)$, $\partial\Omega_2 := (x,y,h_1)$ and $\partial\Omega_3 := (x,y,h_2)$, respectively. A point-like source S at $\mathbf{r}_{\mathrm{S}} := (x_{\mathrm{S}}, y_{\mathrm{S}}, 0)$ generates electrical current. The point-like electrode E at $\mathbf{r}_{\mathrm{E}} := (x_{\mathrm{E}}, y_{\mathrm{E}}, 0)$ measures the electrical potential. Length R_{SE} is the distance between S and E. (B) Schematic illustrating a surface tetrapolar electrical impedance measurement. The current source $(+)$ and sink $(-)$ electrodes are $S_{\pm}$ and the high $(+)$ and low $(-)$ voltage measuring electrodes are $E_{\pm}$. (C) Tetrapolar electrical impedance measurement with linearly aligned current source electrodes $S_{\pm}$ and measuring voltage electrodes $E_{\pm}$. The distance between current and voltage electrodes is A, whereas the distance between voltage electrodes is B.

for further details regarding the mathematical derivation of planar geometrical coefficient in (14).

In this case, the recorded electrical potential difference, apparent electrical impedance and apparent impedance sensitivity in Figure 6 B can be evaluated using (8), (9) and (10) with

$$K_i = \frac{1}{\sqrt{R^2_{S_+E_+} + 4N_i^2}} - \frac{1}{\sqrt{R^2_{S_-E_+} + 4N_i^2}} + \frac{1}{\sqrt{R^2_{S_-E_-} + 4N_i^2}} - \frac{1}{\sqrt{R^2_{S_+E_-} + 4N_i^2}}, \tag{15}$$

where R_{mn} (m) is the distance between $m \in \{S_+, S_-\}$ and $n \in \{E_+, E_-\}$.

If we consider the four electrodes linearly aligned (see Figure 6 C), then the geometrical constant (15) simplifies to

$$K_i = \frac{2}{\sqrt{A^2 + 4N_i^2}} - \frac{2}{\sqrt{(A+B)^2 + 4N_i^2}},$$

with A and B (m) the distances between current and voltage electrodes and inner voltage electrodes, respectively, and G is given in (13).

4. Electrical impedance model in half space with *parallel* circuit-like topology

In this section we consider a nonhomogeneous model $\Lambda^{\mathrm{P}}_{-} \in \mathbb{R}^3_{-}$ consisting of circuit-like *parallel* topology domains. The model assumptions are the same as in Section 3.

4.1. Governing equation

As in Section 3, the governing equation is

$$\nabla \cdot \left(\gamma^{\mathrm{P}}(\mathbf{r}) \nabla U^{\mathrm{P}}(\mathbf{r})\right) = -I\delta(\mathbf{r} - \mathbf{r}_{\mathrm{S}}). \tag{16}$$

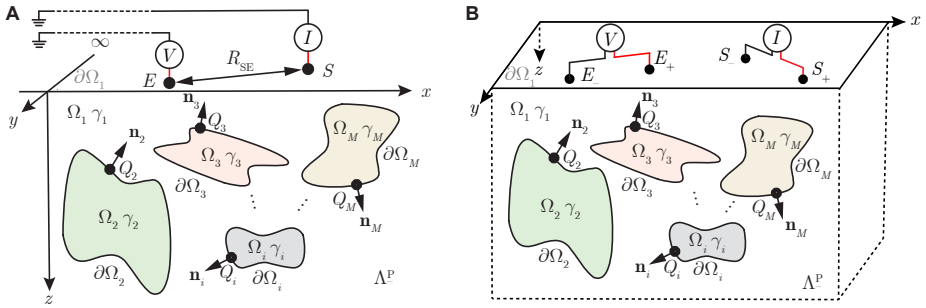

Figure 7. (A) Schematic illustrating a nonhomogeneous tissue modeled as *parallel* circuit-like topology in half space Λ^{P}_{-}. There are M domains Ω_i with $i \in \{1,2,3,\cdots,M\}$ and isotropic admittivity γ_i in Λ^{P}_{-}, where $M-1$ domains Ω_i and $i \neq 1$ are intruded in Ω_1. Surface $\partial\Omega_1 := (x,y,0)$ is the planar boundary of Ω_1, while $\partial\Omega_i$ are outer boundary of Ω_i with an arbitrary surface. A point-like source S at $\mathbf{r}_{\mathrm{S}} := (x_{\mathrm{S}}, y_{\mathrm{S}}, 0)$ on $\partial\Omega_1$ generates electrical current. Another point-like electrode E at $\mathbf{r}_{\mathrm{E}} := (x_{\mathrm{E}}, y_{\mathrm{E}}, 0)$ is a potential recording electrode on $\partial\Omega_1$. Point Q_i $(i \neq 1)$ has coordinates $\mathbf{r}_{\mathrm{Q}_i} := (x_{\mathrm{Q}_i}, y_{\mathrm{Q}_i}, z_{\mathrm{Q}_i})$ on $\partial\Omega_i$, and $\mathbf{n}_i$ is the outward normal vector of $\partial\Omega_i$ at Q_i. Length R_{SE} is the distance between electrode S and E. (B) Schematic illustrating a surface tetrapolar electrical impedance measurement. The current source $(+)$ and sink $(-)$ electrodes are $S_{\pm}$ and the high $(+)$ and low $(-)$ voltage measuring electrodes are $E_{\pm}$ placed on $\partial\Omega_1$, respectively.

where $\gamma^{\mathrm{P}} \in \mathbb{C}$ (S m^{-1}) and $U^{\mathrm{P}} \in \mathbb{C}$ (V) are the nonhomogeneous admittivity and the electrical potential in Λ^{P}_{-}, respectively. The subdomains are arranged as shown in Figure 7 A. According to Table 3, the admittivity distribution $\gamma^{\mathrm{P}}(\mathbf{r})$ can be explicitly expressed as

$$\gamma^{\mathrm{P}}(\mathbf{r}) := \gamma_1 + \sum_{i=2}^{M} (\gamma_i - \gamma_1)\, H(\mathbf{r} + \mathbf{n}_i). \tag{17}$$

Following the same rationale as in Section 3, we can apply the method of images charges to (16), namely

$$\nabla^2 U^{\mathrm{P}}(\mathbf{r}) = -\frac{2I\delta(\mathbf{r}-\mathbf{r}_{\mathrm{S}})}{\gamma^{\mathrm{P}}(\mathbf{r})} - 2\sum_{i=2}^{M} \Gamma_{1|i} \left[\delta(\partial\Omega_i) \frac{\partial U^{\mathrm{P}}(\mathbf{r})}{\partial \mathbf{n}_i} \cdot \mathbf{n}_i + \delta(\partial\overline{\Omega}_i) \frac{\partial U^{\mathrm{P}}(\mathbf{r})}{\partial \overline{\mathbf{n}}_i} \cdot \overline{\mathbf{n}}_i \right], \tag{18}$$

where $\mathbf{r} \neq \mathbf{r}_{\mathrm{S}}$ and $\Gamma_{1|i}$ is the reflection coefficient.

4.2. Electrical potential distribution

Similar to (6), we can introduce a pth-order approximated electrical potential distribution $\widetilde{U}^{\mathrm{P}(p)}(\mathbf{r}) \in \mathbb{C}$ (V) from (18), i.e.,

$$\begin{cases} \widetilde{U}^{\mathrm{P}(p)}(\mathbf{r}) & := U_0(\mathbf{r}) + \sum_{i=2}^{M} U^{\mathrm{P}(p)}_{\Omega_i}(\mathbf{r}) \\ \widetilde{U}^{\mathrm{P}(0)}(\mathbf{r}) & := U_0(\mathbf{r}) \\ \widetilde{U}^{\mathrm{P}(p)}_{\Omega_i}(\mathbf{r}) & := \dfrac{\Gamma_{1|i}}{2\pi} \left[\iint_{\partial\Omega_i} \dfrac{\partial \widetilde{U}^{\mathrm{P}(p-1)}(\mathbf{r}_{\mathrm{Q}_i})}{\partial \mathbf{n}_i} \cdot \mathbf{n}_i \dfrac{\mathrm{d}(\partial\Omega_i)}{|\mathbf{r}-\mathbf{r}_{\mathrm{Q}_i}|} + \iint_{\partial\overline{\Omega}_i} \dfrac{\partial \widetilde{U}^{\mathrm{P}(p-1)}(\mathbf{r}_{\overline{\mathrm{Q}}_i})}{\partial \overline{\mathbf{n}}_i} \cdot \overline{\mathbf{n}}_i \dfrac{\mathrm{d}(\partial\overline{\Omega}_i)}{|\mathbf{r}-\mathbf{r}_{\overline{\mathrm{Q}}_i}|} \right], \end{cases} \tag{19}$$

where $U^{\mathrm{P}}(\mathbf{r}) = \lim_{p\to\infty} \widetilde{U}^{\mathrm{P}(p)}(\mathbf{r})$.

The electrical potential is recorded with electrode E at $\mathbf{r}_{\mathrm{E}} := (x_{\mathrm{E}}, y_{\mathrm{E}}, 0)$ (see Figure 7 A). Then, we can simplify (19) based on the symmetry of the image model with respect to $\partial\Omega_1$ (see Figure 4 B). The 1st-order approximated electrical potential at $\mathbf{r}_{\mathrm{E}}$ is

$$\widetilde{U}^{\mathrm{P}(1)}(\mathbf{r}_{\mathrm{E}}) = \frac{I}{2\pi\gamma_1}\left(\frac{1}{R_{\mathrm{SE}}} + 2\sum_{i=2}^{M} K_{\Omega_i}\Gamma_{1|i}\right). \tag{20}$$

4.3. Apparent electrical impedance

We consider a tetrapolar impedance model as shown in Figure 7 B. Similar to (8), the measured potential difference $\Delta\widetilde{U}^{\mathrm{P}(1)} \in \mathbb{C}$ (V) can be obtained from (20), viz.,

$$\Delta\widetilde{U}^{\mathrm{P}(1)} = \frac{I}{2\pi\gamma_1}\left(G + 2\sum_{i=2}^{M} K_i\Gamma_{1|i}\right). \tag{21}$$

Finally, the 1st-order apparent electrical impedance $Z^{\mathrm{P}(1)} \in \mathbb{C}$ (Ohm) is

$$Z^{\mathrm{P}(1)} := R^{\mathrm{P}(1)} + \tau X^{\mathrm{P}(1)} = \frac{\Delta\widetilde{U}^{\mathrm{P}(1)}}{I} = \frac{1}{2\pi\gamma_1}\left(G + 2\sum_{i=2}^{M} K_i\Gamma_{1|i}\right), \tag{22}$$

where $R^{\mathrm{P}(1)}, X^{\mathrm{P}(1)} \in \mathbb{R}$ (Ohm) are the 1st-order approximated apparent resistance and reactance, respectively.

4.4. Apparent electrical impedance sensitivity to changes in tissue electrical properties

Following the same rationale as in Section 3.4, we can find apparent electrical impedance sensitivity $\Delta Z^{\mathrm{P}(1)}/Z^{\mathrm{P}(1)}$ from (22), namely

$$\frac{\Delta Z^{\mathrm{P}(1)}}{Z^{\mathrm{P}(1)}} \approx \begin{cases} -\frac{\Delta\gamma_i}{\gamma_i}\left(1 - \sum_{k=2}^{M}\frac{2\varpi_{i|k}}{Z^{\mathrm{P}(1)}}\right) & \text{if} \quad i = 1 \\ -\frac{\Delta\gamma_i}{\gamma_i}\frac{2\varpi_{1|i}}{Z^{\mathrm{P}(1)}} & \text{else.} \end{cases} \tag{23}$$

4.5. Case study 3

Here we consider the case study of a nonhomogeneous tissue with $M = 3$ domains where $\Omega_{\{2,3\}}$ are spheres surrounded by tissue Ω_1 (see Figure 8 A). Domain $\Omega_{\{2,3\}}$ is centered at $C_{\{2,3\}}$ with radius $b_{\{2,3\}}$ (m), boundary $\partial\Omega_{\{2,3\}}$. Angle $\theta_{\{2,3\}}$ (rad) is between line segment $|SC_{\{2,3\}}|$ and $|EC_{\{2,3\}}|$ with source S and electrode E on $\partial\Omega_1 : (x, y, 0)$. The 1st-order approximated electrical potential distribution $\widetilde{U}^{\mathrm{SP}(1)}(\mathbf{r}_{\mathrm{E}})$ can be expressed using (20) in Λ_{-}^{P}, where the geometrical coefficient K_{Ω_i} is the same as (11).

Figure 8 B shows the current $S_{\pm}$ and voltage $E_{\pm}$ electrodes for impedance measurement positioned on $\partial\Omega_1$. The electrical potential difference, apparent electrical impedance and apparent impedance sensitivity can be calculated using (21), (22) and (23), where the geometrical coefficients $K_{\{2,3\}}$ are the same as (12). If the voltage and current electrodes

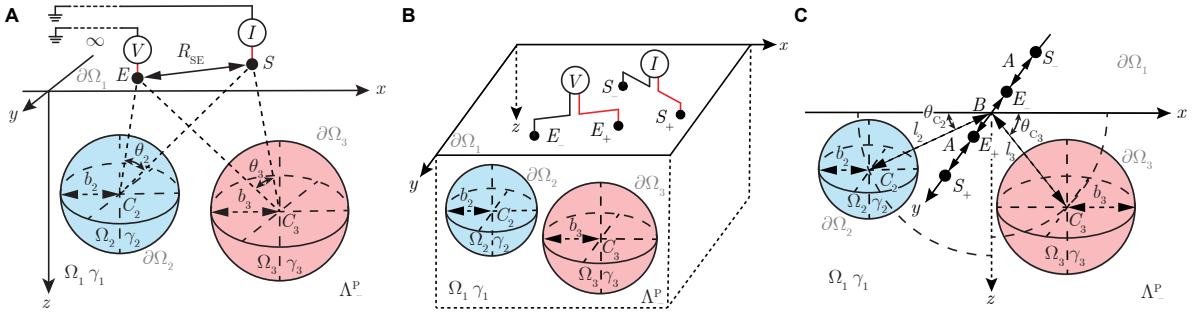

Figure 8. Schematic of case study 3. (A) Nonhomogeneous model $\Lambda^{\mathrm{P}}_{-} \in \mathbb{R}^3_{-}$ representing *parallel* circuit-like topology consisting of two spherical volumes Ω_2 and Ω_3 in domain Ω_1. The admittivity and boundary of domain Ω_i are γ_i and $\partial\Omega_i$, $i \in \{1,2,3\}$, with $\partial\Omega_1 := (x,y,0)$. Spherical domains $\Omega_{\{2,3\}}$ are centered at $C_{\{2,3\}}$ with radii $b_{\{2,3\}}$. A point-like source S at $\mathbf{r}_{\mathrm{S}} := (x_{\mathrm{S}}, y_{\mathrm{S}}, 0)$ generates electrical current. The point-like electrode E at $\mathbf{r}_{\mathrm{E}} := (x_{\mathrm{E}}, y_{\mathrm{E}}, 0)$ measures the electrical potential. Length R_{SE} is the distance between S and E. Angles $\theta_{\{2,3\}}$ are the angle between the line segment $|SC_{\{2,3\}}|$ and $|EC_{\{2,3\}}|$. (B) Schematic illustrating a surface tetrapolar electrical impedance measurement. The current source $(+)$ and sink $(-)$ electrodes are $S_{\pm}$ and the high $(+)$ and low $(-)$ voltage measuring electrodes are $E_{\pm}$. (C) Tetrapolar electrical impedance measurement for case study 3 with linearly aligned current source electrodes $S_{\pm}$ and voltage measuring $E_{\pm}$ electrodes. $C_{\{2,3\}}$ satisfies $|C_{\{2,3\}}S_+| = |C_{\{2,3\}}S_-|$, distance from $C_{\{2,3\}}$ to line segment $|E_+E_-|$ is $l_{\{2,3\}}$, angle between $l_{\{2,3\}}$ and x-axis is $\theta_{\mathrm{C}_{\{2,3\}}}$. The distance between current and voltage electrodes is A, whereas the distance between voltage electrodes is B.

are linearly aligned on $\partial\Omega_1$ and $\left|C_{\{2,3\}}S_+\right| = \left|C_{\{2,3\}}S_-\right|$ as illustrated in Figure 8 C, then distance $l_{\{2,3\}}$ (m) is defined from $C_{\{2,3\}}$ to line segment $|E_+E_-|$ and angle $\theta_{\mathrm{C}_{\{2,3\}}}$ (rad) is the angle between $l_{\{2,3\}}$ and the x-axis. A and B (m) are the distance between current and voltage electrodes and between voltage electrodes, respectively. Finally, K_i and G can be simplified as in (12) and (13).

5. Electrical impedance model in half space with *series-parallel* circuit-like topology

In this section we consider a nonhomogeneous model $\Lambda^{\mathrm{SP}}_{-} \in \mathbb{R}^3_{-}$ consisting of *series-parallel* circuit-like topology domains (see Figure 9 A), i.e., the most general case study considered in here. The model assumptions are the same as in Section 3.

5.1. Governing equation

As in Section 3, the governing equation is

$$\nabla \cdot \left(\gamma^{\mathrm{SP}}(\mathbf{r}) \nabla U^{\mathrm{SP}}(\mathbf{r})\right) = -I\delta(\mathbf{r} - \mathbf{r}_{\mathrm{S}}). \tag{24}$$

where $\gamma^{\mathrm{SP}} \in \mathbb{C}$ (S m^{-1}) and $U^{\mathrm{SP}} \in \mathbb{C}$ (V) are the nonhomogeneous admittivity and the electrical potential in $\Lambda^{\mathrm{SP}}_{-}$, respectively. According to the property of *series-parallel* circuit-like topology listed in Table 3, we can explicitly express the admittivity distribution $\gamma^{\mathrm{SP}}(\mathbf{r})$

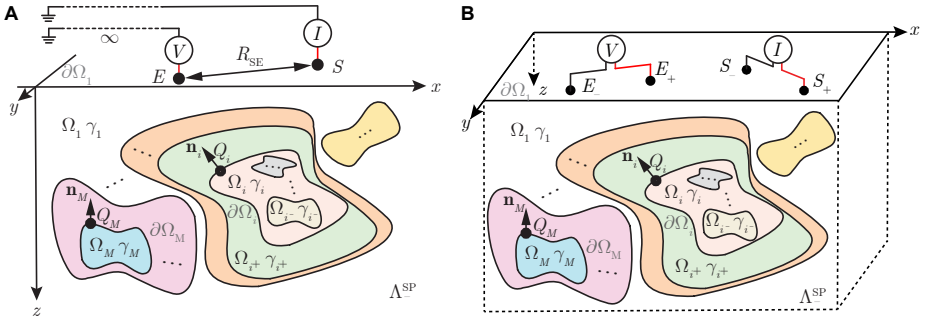

Figure 9. (A) Schematic illustrating a nonhomogeneous tissue modeled as *series-parallel* circuit-like topology in half space Λ_-^{SP}. There are M non-overlapping domains $\Omega_i, i \in \{1,2,3,\cdots,M\}$, with isotropic admittivity γ_i in Λ_-^{SP}. The planar surface $\partial\Omega_1 := (x,y,0)$ is the boundary of Ω_1, whereas $\partial\Omega_i$ are outer boundary of Ω_i. Domains $\Omega_{i^\pm} \in N^{\pm}(\Omega_i)$ are the outer/inner neighbors of Ω_i, where $i^{\pm} \in \{1,2,3,\cdots,i-1,i+1,\cdots,M\}$. A point-like source S at $\mathbf{r}_{\mathrm{S}} := (x_{\mathrm{S}}, y_{\mathrm{S}}, 0)$ on $\partial\Omega_1$ generates electrical current. Another point-like electrode E at position $\mathbf{r}_{\mathrm{E}} := (x_{\mathrm{E}}, y_{\mathrm{E}}, 0)$ is a potential recording electrode on $\partial\Omega_1$. Point Q_i $i \neq 1$ has coordinates $\mathbf{r}_{\mathrm{Q}_i} := (x_{\mathrm{Q}_i}, y_{\mathrm{Q}_i}, z_{\mathrm{Q}_i})$ on $\partial\Omega_i$, and $\mathbf{n}_i$ is the outward normal vector of $\partial\Omega_i$ at Q_i. Length R_{SE} is the distance between S and E. (B) Schematic illustrating a surface tetrapolar electrical impedance measurement. The current source $(+)$ and sink $(-)$ electrodes are $S_\pm$ and the high $(+)$ and low $(-)$ voltage measuring electrodes are $E_\pm$ placed on $\partial\Omega_1$.

as

$$\gamma^{\mathrm{SP}}(\mathbf{r}) := \gamma_1 + \sum_{i=2}^{N} (\gamma_i - \gamma_{i^+}) H(\mathbf{r} + \mathbf{n}_i). \tag{25}$$

Also, we have $|N^+(\Omega_i)| = 1$ from the definition in Table 3. Therefore, the value of i^+ is unique in Λ_-^{SP}. In other words, we can find only one outer neighbor domain Ω_{i^+} enclosing domain Ω_i. Then, the governing equation of *series-parallel* circuit-like topology is deduced based on principle of image charges as

$$\nabla^2 U^{\mathrm{SP}}(\mathbf{r}) = -\frac{2I\delta(\mathbf{r}-\mathbf{r}_{\mathrm{S}})}{\gamma^{\mathrm{SP}}(\mathbf{r})} - 2\sum_{i=2}^{M} \Gamma_{i^+|i} \left[\delta(\partial\Omega_i) \frac{\partial U^{\mathrm{SP}}(\mathbf{r})}{\partial \mathbf{n}_i} \cdot \mathbf{n}_i + \delta(\partial\overline{\Omega}_i) \frac{\partial U^{\mathrm{SP}}(\mathbf{r})}{\partial \overline{\mathbf{n}}_i} \cdot \overline{\mathbf{n}}_i \right], \tag{26}$$

where $\mathbf{r} \neq \mathbf{r}_{\mathrm{S}}$ and $\Gamma_{i^+|i}$ is the reflection coefficient.

5.2. Electrical potential distribution

Following the same rationale as in (6), the pth-order approximated electrical potential distribution $\widetilde{U}^{\mathrm{SP}(p)}(\mathbf{r}) \in \mathbb{C}$ (V) is defined

$$\begin{cases} \widetilde{U}^{\mathrm{SP}(p)}(\mathbf{r}) & := U_0(\mathbf{r}) + \sum_{i=2}^{M} \widetilde{U}_{\Omega_i}^{\mathrm{SP}(p)}(\mathbf{r}) \\ \widetilde{U}^{\mathrm{SP}(0)}(\mathbf{r}) & := U_0(\mathbf{r}) \\ \widetilde{U}_{\Omega_i}^{\mathrm{SP}(p)}(\mathbf{r}) & := \frac{\Gamma_{i^+|i}}{2\pi} \left[\iint_{\partial\Omega_i} \frac{\partial \widetilde{U}^{\mathrm{SP}(p-1)}(\mathbf{r}_{\mathrm{Q}_i})}{\partial \mathbf{n}_i} \cdot \mathbf{n}_i \frac{\mathrm{d}(\partial\Omega_i)}{|\mathbf{r}-\mathbf{r}_{\mathrm{Q}_i}|} + \iint_{\partial\overline{\Omega}_i} \frac{\partial \widetilde{U}^{\mathrm{SP}(p-1)}(\mathbf{r}_{\overline{\mathrm{Q}}_i})}{\partial \overline{\mathbf{n}}_i} \cdot \overline{\mathbf{n}}_i \frac{\mathrm{d}(\partial\overline{\Omega}_i)}{|\mathbf{r}-\mathbf{r}_{\overline{\mathrm{Q}}_i}|} \right] \end{cases} \tag{27}$$

where $U^{\mathrm{SP}}(\mathbf{r}) = \lim_{p\to\infty} \widetilde{U}^{\mathrm{SP}(p)}(\mathbf{r})$. Considering a voltage recording electrode E on $\partial\Omega_1$ (see Figure 9 A), we can simplify the 1st-order approximated electrical potential $\widetilde{U}^{\mathrm{SP}(1)}(\mathbf{r}_{\mathrm{E}})$ as

$$\widetilde{U}^{\mathrm{SP}(1)}(\mathbf{r}_{\mathrm{E}}) = \frac{I}{2\pi\gamma_1}\left(\frac{1}{R_{\mathrm{SE}}} + \sum_{i=2}^{M} K_{\Omega_i}\Gamma_{i^+|i}\right). \tag{28}$$

5.3. Apparent electrical impedance

We consider the surface tetrapolar impedance measurement shown in Figure 9 B. Similar to (8), the 1st-order approximated potential difference $\Delta\widetilde{U}^{\mathrm{SP}(1)} \in \mathbb{C}$ (V) is

$$\Delta\widetilde{U}^{\mathrm{SP}(1)} = \frac{I}{2\pi\gamma_1}\left(G + \sum_{i=2}^{M} K_i\Gamma_{i^+|i}\right). \tag{29}$$

Finally, the 1st-order approximated apparent electrical impedance $Z^{\mathrm{SP}(1)} \in \mathbb{C}$ (Ohm) from (29) is

$$Z^{\mathrm{SP}(1)} := R^{\mathrm{SP}(1)} + \tau X^{\mathrm{SP}(1)} = \frac{\Delta\widetilde{U}^{\mathrm{SP}(1)}}{I} = \frac{1}{2\pi\gamma_1}\left(G + \sum_{i=2}^{M} K_i\Gamma_{i^+|i}\right), \tag{30}$$

where $R^{\mathrm{SP}(1)}, X^{\mathrm{SP}(1)} \in \mathbb{R}$ (Ohm) are the 1st-order approximated apparent resistance and reactance, respectively.

5.4. Apparent electrical impedance sensitivity to changes in tissue electrical properties

Following the same rationale as in Section 3.4, we can find apparent electrical impedance sensitivity $\Delta Z^{\mathrm{SP}(1)}/Z^{\mathrm{SP}(1)}$ from (30), namely

$$\frac{\Delta Z^{\mathrm{SP}(1)}}{Z^{\mathrm{SP}(1)}} \approx \begin{cases} -\frac{\Delta\gamma_i}{\gamma_i}\left[1 - \sum_{i^-\in\{j|\Omega_j\in N^-(\Omega_i)\}} \frac{\varpi_{i|i^-}}{Z}\right] & \text{if} \quad i = 1 \\ -\frac{\Delta\gamma_i}{\gamma_i}\frac{\varpi_{i^+|i}}{Z} & \text{if} \quad i = M \\ -\frac{\Delta\gamma_i}{\gamma_i}\left[\frac{\varpi_{i^+|i}}{Z} + \sum_{i^-\in\{j|\Omega_j\in N^-(\Omega_i)\}} \frac{\varpi_{i|i^-}}{Z}\right] & \text{else.} \end{cases} \tag{31}$$

5.5. Case study 4

Here we consider the case study of a nonhomogeneous model with $M = 4$ domains consisting of two spherical volumes Ω_2 and Ω_3 within a two-layered tissue Ω_1 and Ω_4. The model is defined with $\Omega_1 := 0 < z < h_1$ and $\Omega_4 : \{z > h_1\} - \{\Omega_2 \cup \Omega_3\}$ with boundary $\partial\Omega_1 := (x, y, 0)$ and $\partial\Omega_4 := (x, y, h_1)$, respectively, and where h_1 (m) is the thickness of Ω_1. Domains $\Omega_{\{2,3\}}$ in Ω_4 are modeled as spherical volumes with radii $b_{\{2,3\}}$ (m) and boundaries $\partial\Omega_{\{2,3\}}$ (see Figure 10 A). Angles $\theta_{\{2,3\}}$ (rad) are defined as the angles between the line segments $|SC_{\{2,3\}}|$ and $|EC_{\{2,3\}}|$ with current source S and voltage electrode E on $\partial\Omega_1$.

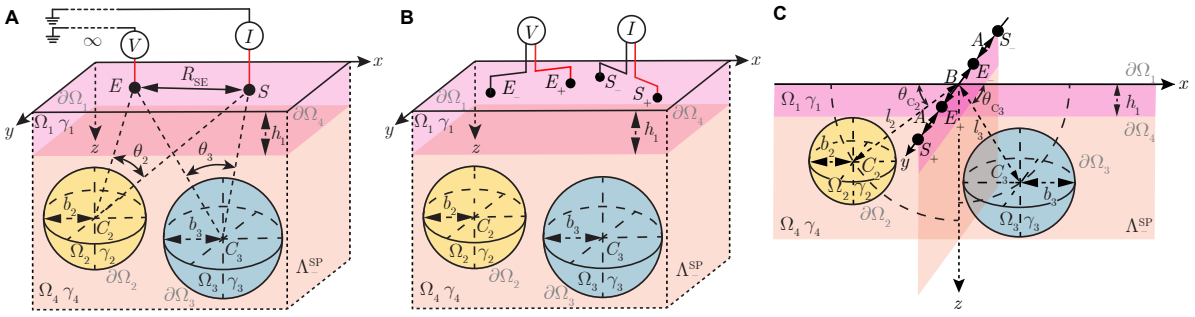

Figure 10. Schematic of case study 4. (A) Nonhomogeneous model $\Lambda^{\mathrm{SP}}_{-} \in \mathbb{R}^3_{-}$ with *series-parallel* circuit-like topology consisting of two-layered domains Ω_1 and Ω_4 and two spherical volumes Ω_2 and Ω_3 in Ω_4. The admittivity and boundary of Ω_i are γ_i and $\partial\Omega_i$, $i \in \{1,2,3,4\}$, with $\partial\Omega_1 := (x,y,0)$ and $\partial\Omega_4 := (x,y,h_1)$. The spherical domains $\Omega_{\{2,3\}}$ are centered at $C_{\{2,3\}}$ with radii $b_{\{2,3\}}$. A point-like source S at $\mathbf{r}_{\mathrm{S}} := (x_{\mathrm{S}}, y_{\mathrm{S}}, 0)$ generates electrical current. A point-like electrode E at $\mathbf{r}_{\mathrm{E}} := (x_{\mathrm{E}}, x_{\mathrm{E}}, 0)$ measures the electrical potential. Length R_{SE} is the distance between S and E, angle $\theta_{\{2,3\}}$ is the angle between the line segment $|SC_{\{2,3\}}|$ and $|EC_{\{2,3\}}|$. (B) Schematic illustrating a surface tetrapolar electrical impedance measurement. The current source $(+)$ and sink $(-)$ electrodes are $S_{\pm}$ and the high $(+)$ and low $(-)$ voltage measuring electrodes are $E_{\pm}$. (C) Tetrapolar electrical impedance measurement for case study 4 with linearly aligned current source electrodes $S_{\pm}$ and measuring voltage $E_{\pm}$ electrodes. The center $C_{\{2,3\}}$ satisfies $|C_{\{2,3\}}S_+| = |C_{\{2,3\}}S_-|$. The distance from $C_{\{2,3\}}$ to line segment $|E_+E_-|$ is $l_{\{2,3\}}$, the angle between $l_{\{2,3\}}$ and x-axis is $\theta_{C_{\{2,3\}}}$. The distance between current and voltage electrodes is A, whereas the distance between voltage electrodes is B.

The 1st-order approximated electrical potential recorded can determined using (28) using the geometrical coefficients $K_{\Omega_{\{2,3\}}}$ and K_{Ω_4} defined in (11) and (14), respectively. The 1st-order approximated electrical potential difference, apparent electrical impedance and apparent impedance sensitivity shown in Figure 10 B can be evaluated using (29), (30) and (31) where $K_{\{2,3\}}$ and K_4 are the same as in (12) and (15). If the electrodes are linearly aligned on $\partial\Omega_1$ and $\left|C_{\{2,3\}}S_+\right| = \left|C_{\{2,3\}}S_-\right|$ (see Figure 10 C), then the distances $l_{\{2,3\}}$ (m) are defined from $C_{\{2,3\}}$ to the line segment $|E_+E_-|$ and the angles $\theta_{C_{\{2,3\}}}$ (rad) are the angles between $l_{\{2,3\}}$ and the x-axis. A and B (m) are the distance between current and voltage electrodes and between voltage electrodes, respectively. Finally, the same simplifications can be made for $K_{\{2,3\}}$ as in (12), K_4 as in (15), and G as in (13).

6. Extension: Electrical impedance model in full space with *series-parallel* circuit-like topology

In this section we extend the framework in Section 5 to full space $\Lambda^{\mathrm{SP}} \in \mathbb{R}^3$ (see Figure 11 A). This generalization represents the model when the electrodes are not on the surface of the tissue but surrounded by tissue as for example when using penetrating electrodes. The model assumptions in Section 3 that apply in full space are (1) to (3).

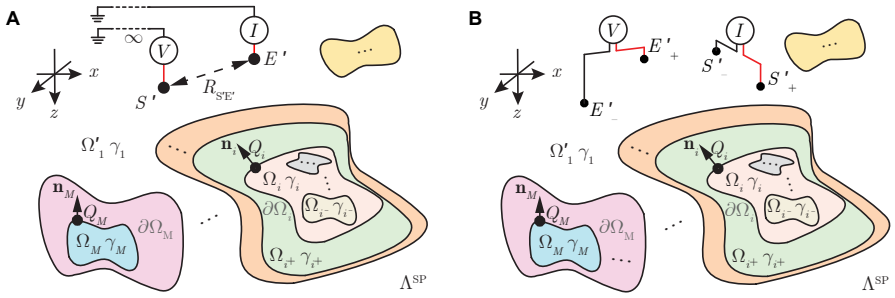

Figure 11. (A) Schematic illustrating a nonhomogeneous tissue modeled as *series-parallel* circuit-like topology in full space $\Lambda \in \mathbb{R}^3$. There are M non-overlapping domains Ω'_1 and Ω_i, $i \in \{2,3,4,\cdots,M\}$, with isotropic admittivity γ_1 and γ_i, respectively. Surface $\partial\Omega_i$ is the outer boundary of Ω_i. Domains $\Omega_{i^\pm} \in N^{\pm}(\Omega_i)$ are the outer/inner neighbors of Ω_i, where $i^{\pm} \in \{1,2,3,\cdots,i-1,i+1,\cdots,M\}$. A point-like source S' at $\mathbf{r}_{S'} := (x_{S'}, y_{S'}, z_{S'})$ in Ω'_1 generates electrical current. A point-like electrode E' at $\mathbf{r}_{E'} := (x_{E'}, y_{E'}, 0)$ measures the electrical potential. Point Q'_i, $i \neq 1$, is at $\mathbf{r}_{Q_i} := (x_{Q_i}, y_{Q_i}, z_{Q_i})$ on $\partial\Omega_i$, and $\mathbf{n}_i$ is the outward normal vector of $\partial\Omega_i$ at Q_i. Length $R_{S'E'}$ is the distance between S' and E'. (B) Schematic illustrating a surface tetrapolar electrical impedance measurement. The current source $(+)$ and sink $(-)$ electrodes are $S'_\pm$ and the high $(+)$ and low $(-)$ voltage measuring electrodes are $E'_\pm$.

6.1. Governing equation

As in Section 3, the governing equations in Λ^{SP} is

$$\nabla \cdot \left(\gamma'^{SP}(\mathbf{r}) \nabla U'^{SP}(\mathbf{r}) \right) = -I\delta(\mathbf{r} - \mathbf{r}_S). \tag{32}$$

where $\gamma'^{SP} \in \mathbb{C}$ (S m^{-1}) and $U'^{SP} \in \mathbb{C}$ (V) are the nonhomogeneous admittivity and the electrical potential in Λ^{SP}, respectively. The model Λ^{SP} contains domains Ω'_1 and Ω_i, $i \neq 1$, as illustrated in Figure 11 A, where $\Omega'_1 \cup \left(\bigcup_{2\leq i\leq M} \Omega_i\right) = \Lambda^{SP}$. Of note, the admittivity distribution in Λ^{SP} shares the same definition as that in Λ^{SP}_- in (25), i.e., $\gamma'^{SP}(\mathbf{r}) = \gamma^{SP}(\mathbf{r})$. We consider a point-like source S' at $\mathbf{r}_{S'} := (x_{S'}, y_{S'}, z_{S'})$ in Ω'_1. The governing equation can be directly deduced from (32), namely

$$\nabla^2 U'^{SP}(\mathbf{r}) = -\frac{I\delta(\mathbf{r} - \mathbf{r}_{S'})}{\gamma'^{SP}} - 2\sum_{i=2}^{M} \Gamma_{i^+|i}\,\delta(\partial\Omega_i) \frac{\partial U'^{SP}(\mathbf{r})}{\partial \mathbf{n}_i} \cdot \mathbf{n}_i. \tag{33}$$

where $\mathbf{r} \neq \mathbf{r}_{S'}$ and reflection coefficient $\Gamma_{i^+|i}$ has the same definition as in Section 5.

6.2. Electrical potential distribution

Following the same rationale as in (6), one can obtain the pth-order approximated electrical potential distribution $\widetilde{U}'^{SP(p)}(\mathbf{r}) \in \mathbb{C}$ (V) in Λ^{SP} as

$$\begin{cases} \widetilde{U}'^{SP(p)}(\mathbf{r}) & := \frac{I}{4\pi\gamma_1 \left|\mathbf{r} - \mathbf{r}_{S'}\right|} + \sum_{i=2}^{M} \widetilde{U}'^{SP(p)}_{\Omega_i}(\mathbf{r}) \\ \widetilde{U}'^{SP(0)}(\mathbf{r}) & := \frac{I}{4\pi\gamma_1 \left|\mathbf{r} - \mathbf{r}_{S'}\right|} \\ \widetilde{U}'^{SP(p)}_{\Omega_2}(\mathbf{r}) & := \frac{\Gamma_{i^+|i}}{2\pi} \iint_{\partial\Omega_i} \frac{\partial \widetilde{U}'^{SP(p-1)}(\mathbf{r}_{Q_i})}{\partial \mathbf{n}_i} \cdot \mathbf{n}_i \frac{\mathrm{d}(\partial\Omega_2)}{\left|\mathbf{r} - \mathbf{r}_{Q_i}\right|}, \end{cases} \tag{34}$$

where $U'^{\mathrm{SP}}(\mathbf{r}) = \lim_{p\to\infty} \widetilde{U}'^{\mathrm{SP}(p)}(\mathbf{r})$. A point-like electrode E' at $\mathbf{r}_{\mathrm{E}'} := (x_{\mathrm{E}'}, y_{\mathrm{E}'}, z_{\mathrm{E}'})$ measures the electrical potential (see Figure 11 A). Then, the 1st-order electrical potential $\widetilde{U}'^{\mathrm{SP}(1)}(\mathbf{r}_{\mathrm{E}'})$ can be simplified from (34) as

$$\widetilde{U}'^{\mathrm{SP}(1)}(\mathbf{r}_{\mathrm{E}'}) = \frac{I}{4\pi\gamma_1}\left(\frac{1}{R_{\mathrm{S}'\mathrm{E}'}} + \sum_{i=2}^{M} K'_{\Omega_i}\Gamma_{i^+|i}\right), \tag{35}$$

where $R_{\mathrm{S}'\mathrm{E}'}$ (m) is the distance between source S' and electrode E', geometrical coefficient K'_{Ω_i} (m^{-1}) maintains the same definition as K_{Ω_i} in (7) replacing S, E with S', E'.

6.3. Apparent impedance measurement

We consider a tetrapolar electrical impedance measurement shown in Figure 11 B. The electrodes of current source $(+)$ and sink $(-)$ are $S'_{\pm}$ and the measuring electrodes of high $(+)$ and low $(-)$ potential are $E'_{\pm}$. Similar to (8), we can deduce the 1st-order approximated potential difference $\Delta\widetilde{U}'^{\mathrm{SP}(1)} \in \mathbb{C}$ (V) as

$$\Delta\widetilde{U}'^{\mathrm{SP}(1)} = \frac{I}{4\pi\gamma_1}\left(G' + \sum_{i=2}^{M} K'_i\Gamma_{i^+|i}\right), \tag{36}$$

where geometrical constant $G' := 1/R'_{++} - 1/R'_{+-} + 1/R'_{--} - 1/R'_{-+}$ (m^{-1}), in which R'_{wv} (m) is the distance between electrode S'_v and E'_w with $w, v \in \{+,-\}$, geometrical coefficient K'_i (m^{-1}) maintains the same definition as K_i in (8) replacing S, E with S', E'. Finally, the 1st-order approximated apparent electrical impedance $Z'^{\mathrm{SP}(1)} \in \mathbb{C}$ (Ohm) from (36) gives

$$Z'^{\mathrm{SP}(1)} := R'^{\mathrm{SP}(1)} + \tau X'^{\mathrm{SP}(1)} = \frac{\Delta\widetilde{U}'^{\mathrm{SP}(1)}}{I} = \frac{1}{4\pi\gamma_1}\left(G' + \sum_{i=2}^{M} K'_i\Gamma_{i^+|i}\right), \tag{37}$$

where $R'^{\mathrm{SP}(1)}, X'^{\mathrm{SP}(1)} \in \mathbb{R}$ (Ohm) are the 1st-order approximated apparent resistance and reactance, respectively.

6.4. Apparent electrical impedance sensitivity to changes in tissue electrical properties

Following the same rationale as in Section 3.4, we can find apparent electrical impedance sensitivity $\Delta Z'^{\mathrm{SP}(1)}/Z'^{\mathrm{SP}(1)}$ from (37), namely

$$\frac{\Delta Z'^{\mathrm{SP}(1)}}{Z'^{\mathrm{SP}(1)}} \approx \begin{cases} -\frac{\Delta\gamma_i}{\gamma_i}\left[1 - \sum_{i^-\in\{j|\Omega_j\in N^-(\Omega_i)\}} \frac{\varpi'_{i|i^-}}{Z'^{\mathrm{SP}(1)}}\right] & \text{if} \quad i = 1 \\ -\frac{\Delta\gamma_i}{\gamma_i}\frac{\varpi'_{i^+|i}}{Z'^{\mathrm{SP}(1)}} & \text{if} \quad i = M \\ -\frac{\Delta\gamma_i}{\gamma_i}\left[\frac{\varpi'_{i^+|i}}{Z} + \sum_{i^-\in\{j|\Omega_j\in N^-(\Omega_i)\}} \frac{\varpi'_{i|i^-}}{Z'^{\mathrm{SP}(1)}}\right] & \text{else.} \end{cases} \tag{38}$$

where $\varpi'_{j|i}$ (Ohm) maintains the same definition as $\varpi_{j|i}$ in (10) replacing the geometrical coefficient K_i in half space with K'_i in full space.

Table 2. Finite element model simulation settings shown in Figure 12.

Symbol	Unit	Case study 1	Case study 2	Case study 3	Case study 4 & 5
I	mA	1	1	1	1
$\omega\cdot(2\pi)^{-1}$	kHz	50	50	50	50
A	mm	3	3	3	3
B	mm	8	8	8	8
l_2	mm	[6,14]	-	[6,14]	[6,14]
l_3	mm	[6,14]	-	7	{7,8,10}
b_2	mm	[2,6]	-	[2,6]	[2,6]
b_3	mm	[1,5]	-	4	{2,3,4}
θ_{C_2}	°	-	-	[40,60]	[40,60]⋃{70}
θ_{C_3}	°	-	- 45	{45,70}	
h_1	mm	-	[1,5]	-	[1,5]
h_2	mm	-	[1,5]	-	-
σ_1	S m^{-1}	1	1	1	
σ_2	S m^{-1}	[0.5,1.5]	[0.5,1.5]	[0.5,1.5]	[0.5,1.5]
σ_3	S m^{-1}	[0.5,1.5]	[0.5,1.5]	[0.5,1.5]	[0.5,1.5]
σ_4	S m^{-1}	-	-	-	[0.5,1.5]
ε_{r1} ($\times10^5$)	-	1	1	1	1
ε_{r2} ($\times10^5$)	-	[0.5,1.5]	[0.5,1.5]	[0.5,1.5]	[0.5,1.5]
ε_{r3} ($\times10^5$)	-	[0.5,1.5]	[0.5,1.5]	[0.5,1.5]	[0.5,1.5]
ε_{r4} ($\times10^5$)	-	-	-	-	[0.5,1.5]

6.5. Case study 5

Here we consider the case study of nonhomogeneous tissue with $M = 4$ domains consisting of two spherical volumes Ω_2 and Ω_3 within two half-space tissue Ω_1' and Ω_4. Of note, all the geometrical configurations of case study 5 are modeled the same as case study 4 (see Figure 10) except Ω_1 in Λ_-^{SP} is extended to $\Omega_1' := z > h_1$ in Λ^{SP}. The source $(+)$ and sink $(-)$ current source and high $(+)$ and low $(-)$ potential recording electrodes are $S_\pm'$ and $E_\pm'$, respectively. The 1st-order approximation of the electrical potential $\widetilde{U}'^{\mathrm{SP}(1)}$, electrical potential difference $\Delta\widetilde{U}'^{\mathrm{SP}(1)}$, apparent electrical impedance $Z'^{\mathrm{SP}(1)}$ and apparent impedance sensitivity $\Delta Z'^{\mathrm{SP}(1)}/Z'^{\mathrm{SP}(1)}$ can be formulated by (35), (36), (37) and (38), respectively, where the geometrical parameters $K'_{\Omega_{\{2,3\}}}$, $K'_{\{2,3\}}$, G', K'_{Ω_4} and K'_4 keep the same expressions as in (11), (12), (13), (14) and (15) replacing S, E with S', E'.

7. Materials and methods

We confirm the accuracy of our theoretical framework through numerical (MATLAB, The Mathworks, Natick, MA, USA) and finite element model (FEM, Comsol Multiphysics, Comsol, Inc., Burlington, MA, USA) simulations. The model simulation settings are summarized in Table 2. In the model, geometrical parameters l_2, b_2, b_3, θ_{C_2}, h_1, h_2 and electrical property parameters σ_2, σ_3, ε_{r2}, ε_{r2} are variables in our simulations. Additional FEM simulation parameters are provided next.

7.1. Finite element model simulations

Figure 12 illustrates the three-dimensional FEM models developed to validate our theoretical framework. For the simulations of case study 1 (Figure 12 A) and case study 3 (Figure

12 B), the domain Ω_1 is modeled as a cuboid with dimensions width $\times$ length $\times$ height $140 \times 140 \times 100$ mm. For the simulations of case study 2 (Figure 12 C), Ω_1 and Ω_2 are modeled as cuboids with dimensions $140 \times 140 \times h_1$ mm and $140 \times 140 \times h_2$ mm, whereas Ω_3 has dimensions $140 \times 140 \times (100 - h_1)$ mm. For the simulations of case study 4 (Figure 12 D) and case study 5 (Figure 12 E), the domain Ω_4 is modeled as a cuboid with dimensions width $\times$ length $\times$ height $140 \times 140 \times (100 - h_1)$ mm, where as the domains Ω_1 and Ω_1' are modeled as cuboids with dimensions width $\times$ length $\times$ height $140 \times 140 \times h_1$ mm and $140 \times 140 \times (100 + h_1)$ mm, respectively. The dimensions of the domain satisfy simulation results are not affected by the domain boundary, in other words, the domain can be considered half space and full space. Adaptive mesh is used to ensure simulation accuracy by having a finer spatial mesh resolution near the electrodes and boundary between domains, while being a coarser mesh spatial resolution elsewhere. The minimum mesh element size is 10^{-4} mm, the maximum element growth rate is 1.2 and the curvature factor is 0.2. The total elements for the model of cases 1, 2, 3 are 192,108; 1,654,653 and 206,945, respectively, whereas for case 4 and 5 are 1,174,848 and 353,545, respectively. BiCGStab solver is used to run the simulations and the relative tolerance is set as 0.001.

7.2. Apparent electrical impedance

The 1st-rder approximated apparent impedance is computed in Matlab for *series*, *parallel*, *series-parallel* circuit-like topology in half space and full space using (9), (22), (30) and (37). Since the 1st-order approximated electrical potential depends on the reflection coefficient between domains with different admittivity properties, we evaluate the accuracy of our predictions to changes in the conductivity and (relative) permittivity properties defined as $\delta_{\sigma_i} := (\sigma_i - \sigma_1)/\sigma_1$ and $\delta_{\varepsilon_i} := (\varepsilon_i - \varepsilon_1)/\varepsilon_1$, respectively. Finally, the relative error between the theoretical and FEM simulated apparent resistance and reactance results is calculated as $e_{\mathrm{R}} := (R_{\mathrm{Theory}} - R_{\mathrm{FEM}})/R_{\mathrm{FEM}}$ and $e_{\mathrm{X}} := (X_{\mathrm{Theory}} - X_{\mathrm{FEM}})/X_{\mathrm{FEM}}$, respectively.

8. Simulation results

8.1. Apparent electrical impedance of series topology

Figures 13 (A, B and C) and 14 (A and B) compare the 1st-order approximated numerical and FEM-simulated apparent impedance for case study 1 and case study 2, respectively. Figures 13 (D, E, F and G) and 14 (C, D, E and F) plot the relative error distribution of apparent resistance and reactance values varying the conductivity and relative permittivity properties of tissue from -50% to 50% while keeping the rest of model parameters constant.

Overall, theoretical and FEM-simulated results are in good agreement with varying depth of spherical center from 6 to 14 mm in case study 1 (Figure 13 A); the 1st-order approximation also being able to detect spherical changes shown in Figure 13 B and C. In addition, impedance results for case study 2 shown in Figure 14 A, B are in good agreement changing the tissue thickness from 1 to 5 mm. The accuracy of the 1st-order approximated apparent resistance (Figure 13 D, F) and reactance (Figure 13 E, G) predictions for case study

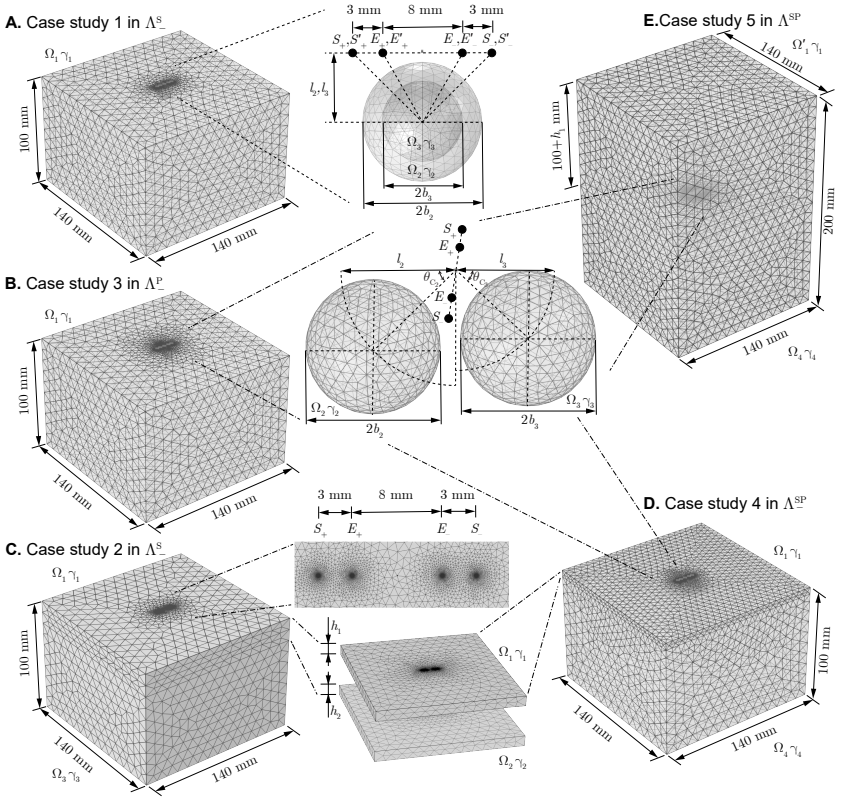

Figure 12. Three-dimensional views of the finite element models (FEM) developed to validate the accuracy of our theoretical impedance framework of nonhomogeneous tissue considering: (A), case study 1 in half space with *series* circuit-like topology; (B), case study 3 in half space with *parallel* circuit-like topology; (C), case study 2 in half space with *series* circuit-like topology; case study 4 and case study 5 with *series-parallel* circuit-like topology in half space (D) and full space (E). The current source (+) and sink (−) electrodes are $S\pm$, $S'\pm$ and the high (+) and low (−) potential recording electrodes $E\pm$, $E'\pm$ measure the apparent electrical impedance. We refer the reader to Table 2 for additional model setting parameters.

1 are $< 1.5\%$ and $< 5\%$, respectively. For case study 2, the maximum error is $< 2\%$ for resistance (Figure 14 C and E) and $< 4\%$ for reactance (Figure 14 D and F).

8.2. Apparent electrical impedance of parallel topology

Figure 15 compares the 1st-order approximated numerical and FEM-simulated apparent impedance for case study 3. The results show the theoretical framework can accurately model changes in position and size of the spherical domain (Figure 15 A, B, C). The maximum error of apparent resistance and reactance to changes in conductivity and relative permittivity properties are $< 0.1\%$ and $< 0.5\%$, respectively (Figure 15 D, E). Interestingly, if the dimension of the spherical volume and the relative distance from the spherical domain to current sources and voltage electrodes are kept constant (see Figure 15 C), then changing the azimuth angle of the spherical volume has no influence on the apparent impedance.

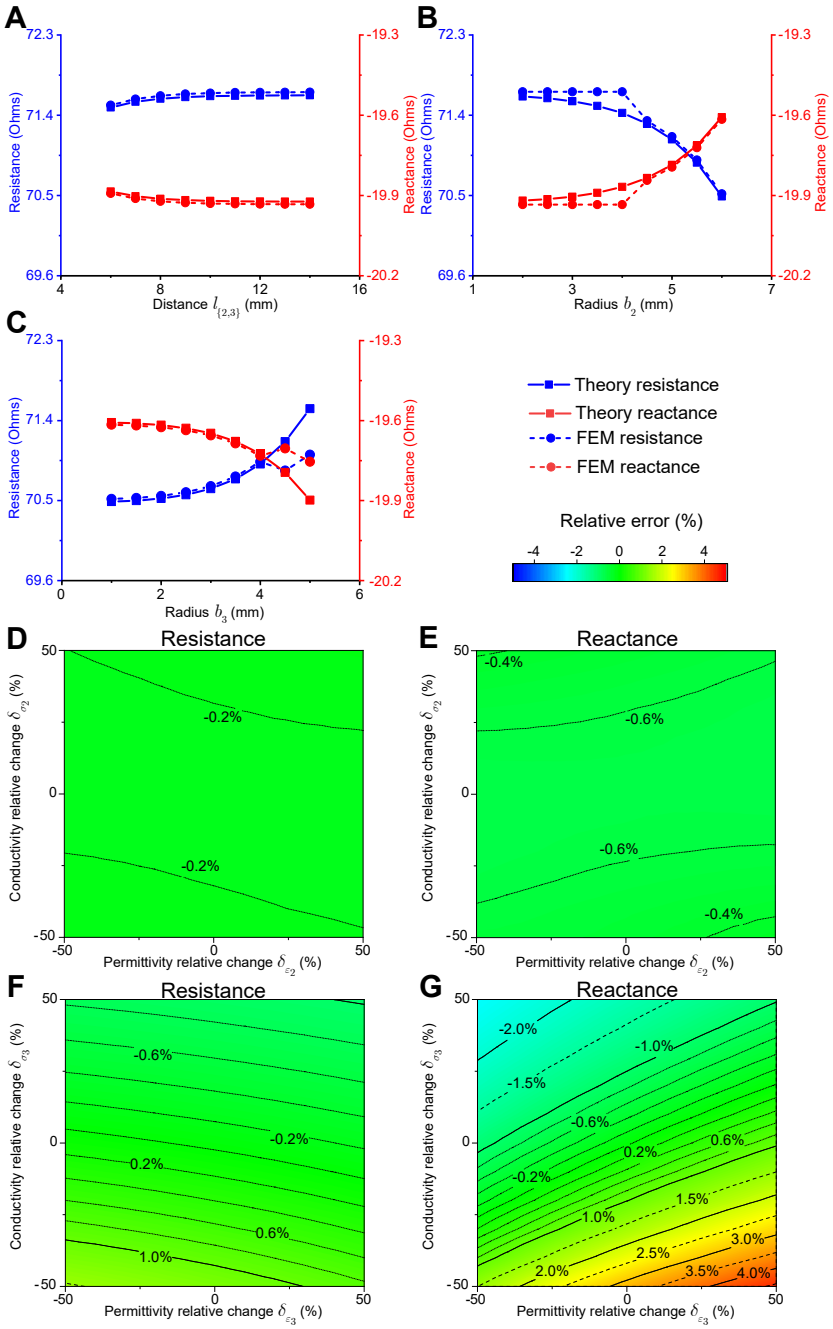

Figure 13. Analytical and FEM-simulated impedance results of case study 1 (see Figure 5 C and Figure 12 A). Theoretical (solid line) and FEM-simulated (dotted line) resistance and reactance with $l_{\{2,3\}} = [6, 14]$ mm, $b_2 = 4$ mm and $b_3 = 3$ mm (A); $b_2 = [2, 6]$ mm, $l_{\{2,3\}} = 7$ mm and $b_3 = 1$ mm (B); $b_3 = [1, 5]$ mm, $l_{\{2,3\}} = 7$ mm and $b_2 = 6$ mm (C). Additional simulation setting parameters: $\sigma_1 = 1\,\mathrm{S\,m^{-1}}$, $\varepsilon_{r2} = 1 \times 10^5$ (dimensionless), $\sigma_2 = 1.1\,\mathrm{S\,m^{-1}}$, $\varepsilon_{r2} = 1.1 \times 10^5$ (dimensionless), $\sigma_3 = 0.9\,\mathrm{S\,m^{-1}}$, $\varepsilon_{r3} = 0.9 \times 10^5$ (dimensionless). (D, E) Relative resistance and reactance errors changing the admittivity of domain Ω_2 (i.e., δ_{σ_2} and δ_{ε_2}) with $\sigma_3 = 1.1\,\mathrm{S\,m^{-1}}$, $\varepsilon_{r3} = 0.9 \times 10^5$ (dimensionless). (F, G) Relative resistance and reactance errors changing the admittivity of domain Ω_3 (i.e, δ_{σ_3}, δ_{ε_3}) with $\sigma_2 = 1.1\,\mathrm{S\,m^{-1}}$, $\varepsilon_{r2} = 0.9 \times 10^5$ (dimensionless). Additional simulation setting parameters: $\sigma_1 = 1\,\mathrm{S\,m^{-1}}$, $\varepsilon_{r2} = 1 \times 10^5$ (dimensionless), $l_{\{2,3\}} = 9$ mm, $b_2 = 6$ mm, $b_3 = 5$ mm.

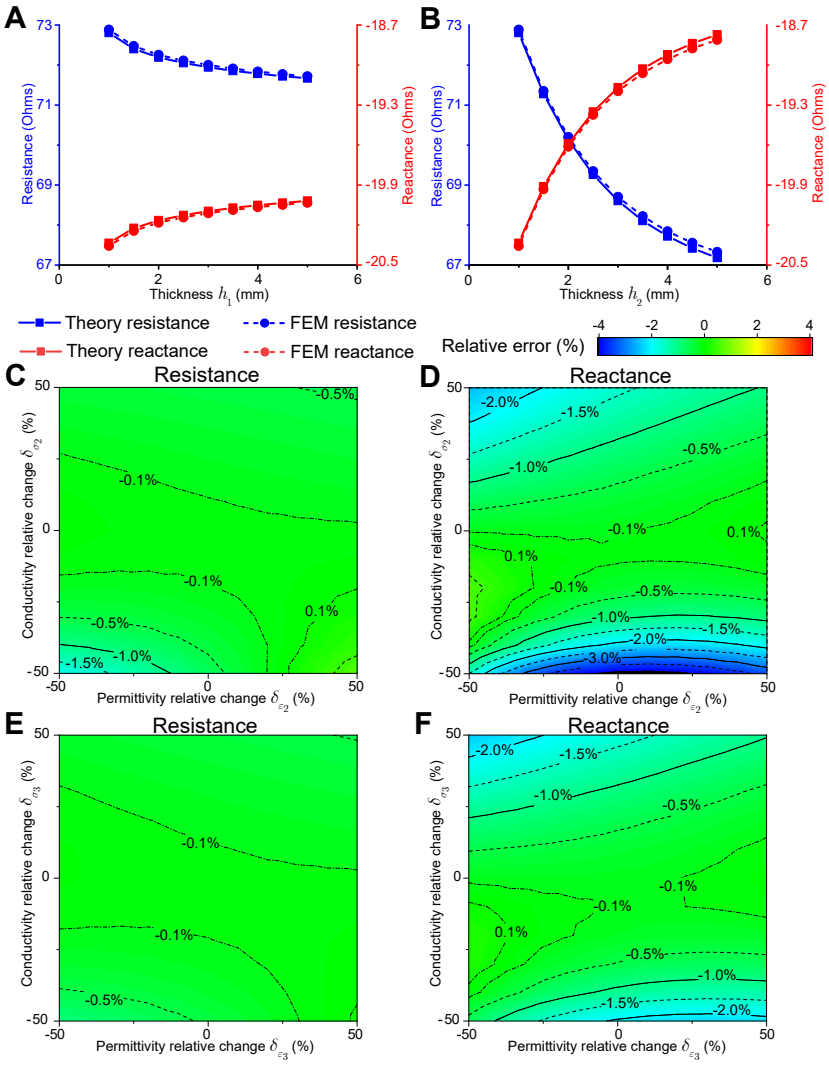

Figure 14. Analytical and FEM-simulated impedance results of case study 2 (see Figure 6 C and Figure 12 C). Theoretical (solid line) and FEM-simulated (dotted line) resistance and reactance with $h_1 = [1,5]$ mm, $h_2 = 1$ mm (A); $h_1 = 1$ mm, $h_2 = [1,5]$ mm (B). Additional simulation parameters: $\sigma_1 = 1\,\mathrm{S\,m^{-1}}$, $\varepsilon_{r2} = 1 \times 10^5$ (dimensionless), $\sigma_2 = 1.1\,\mathrm{S\,m^{-1}}$, $\varepsilon_{r2} = 1.1 \times 10^5$ (dimensionless), $\sigma_3 = 0.9\,\mathrm{S\,m^{-1}}$, $\varepsilon_{r3} = 0.9 \times 10^5$ (dimensionless). (C, D) Relative resistance and reactance errors changing the admittivity of domain Ω_2 (i.e, δ_{σ_2}, δ_{ε_2}) with $\sigma_3 = 1.1\,\mathrm{S\,m^{-1}}$, $\varepsilon_{r3} = 0.9 \times 10^5$ (dimensionless). (E, F) Relative resistance and reactance errors changing the admittivity of domain Ω_3 (i.e, δ_{σ_3}, δ_{ε_3}) with $\sigma_2 = 1.1\,\mathrm{S\,m^{-1}}$, $\varepsilon_{r2} = 0.9 \times 10^5$ (dimensionless). Additional simulation parameters: $\sigma_1 = 1\,\mathrm{S\,m^{-1}}$, $\varepsilon_{r2} = 1 \times 10^5$ (dimensionless), $h_1 = 2$ mm, $h_2 = 2$ mm.

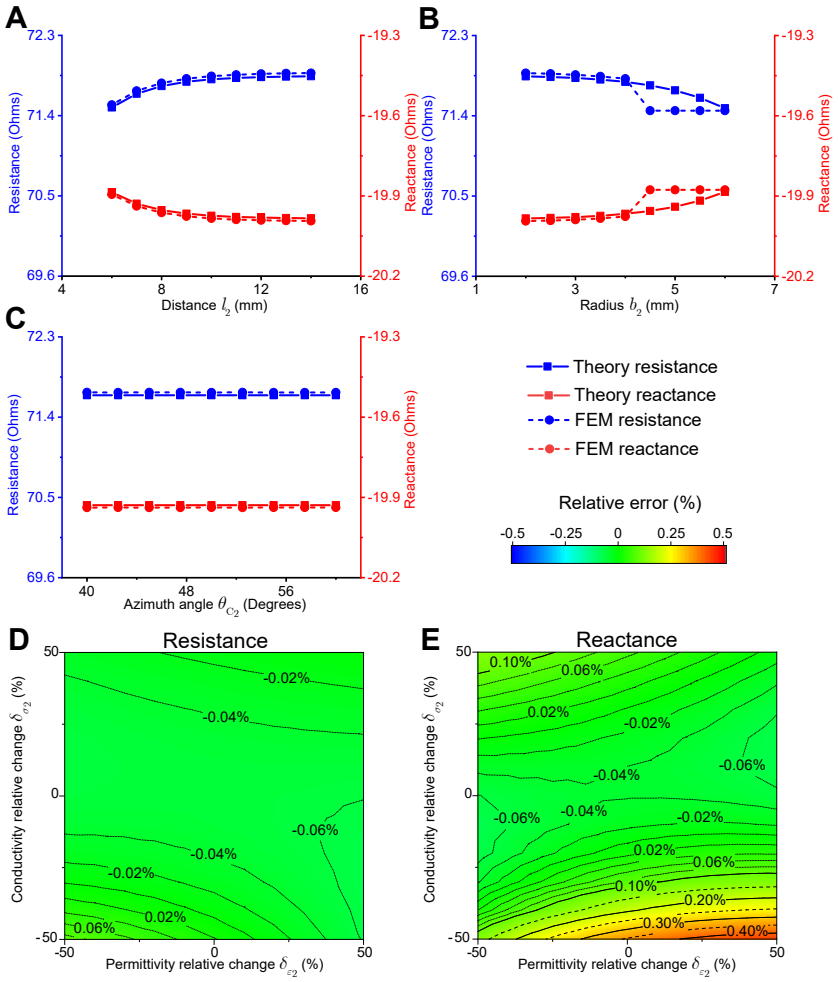

Figure 15. Analytical and FEM-simulated impedance results of case study 3 (see Figure 8 C and Figure 12 B). Theoretical (solid line) and FEM-simulated (dotted line) resistance and reactance with $l_2 = [6,14]$ mm, $l_3 = 7$ mm, $b_{\{2,3\}} = 4$ mm, $\theta_{C_{\{2,3\}}} = 45$ degrees (A); $b_2 = [2,6]$ mm, $b_3 = 4$ mm, $l_{\{2,3\}} = 7$ mm, $\theta_{C_{\{2,3\}}} = 45$ degrees (B); $\theta_{C_2} = [40°, 60°]$, $\theta_{C_3} = 45°$, $l_{\{2,3\}} = 7$ mm, $b_{\{2,3\}} = 4$ mm (C). Additional simulation setting parameters: $\sigma_1 = 1\,\mathrm{S\,m^{-1}}$, $\varepsilon_{r2} = 1 \times 10^5$ (dimensionless), $\sigma_2 = 1.1\,\mathrm{S\,m^{-1}}$, $\varepsilon_{r2} = 1.1 \times 10^5$ (dimensionless), $\sigma_3 = 0.9\,\mathrm{S\,m^{-1}}$, $\varepsilon_{r3} = 0.9 \times 10^5$ (dimensionless). (D, E) Relative resistance and reactance errors changing the admittivity of domain Ω_2 (i.e, δ_{σ_2}, δ_{ε_2}) with $\sigma_1 = 1\,\mathrm{S\,m^{-1}}$, $\varepsilon_{r2} = 1 \times 10^5$ (dimensionless), $\sigma_3 = 1.1\,\mathrm{S\,m^{-1}}$, $\varepsilon_{r3} = 0.9 \times 10^5$ (dimensionless), $l_{\{2,3\}} = 7$ mm, $b_2 = 4$ mm, $\theta_{C_{\{2,3\}}} = 45°$.

8.3. Apparent electrical impedance of series-parallel topology

Figures 16 and 17 compare the 1st-order approximated numerical and FEM-simulated apparent impedance for case study 4 in half space and case study 5 in full space, respectively. In both half and full space, there is good agreement with varying thickness (Figure 16 A and Figure 17 A), dimensions of the spherical domains (Figure 16 B and Figure 17 B), and relative distance to the spherical center (Figure 16 C and Figure 17 C). Figure 16 D and Figure 17 D reveal that the azimuth angle of the spherical volume does not contribute to the apparent impedance. The maximum errors changing the conductivity and relative permittivity

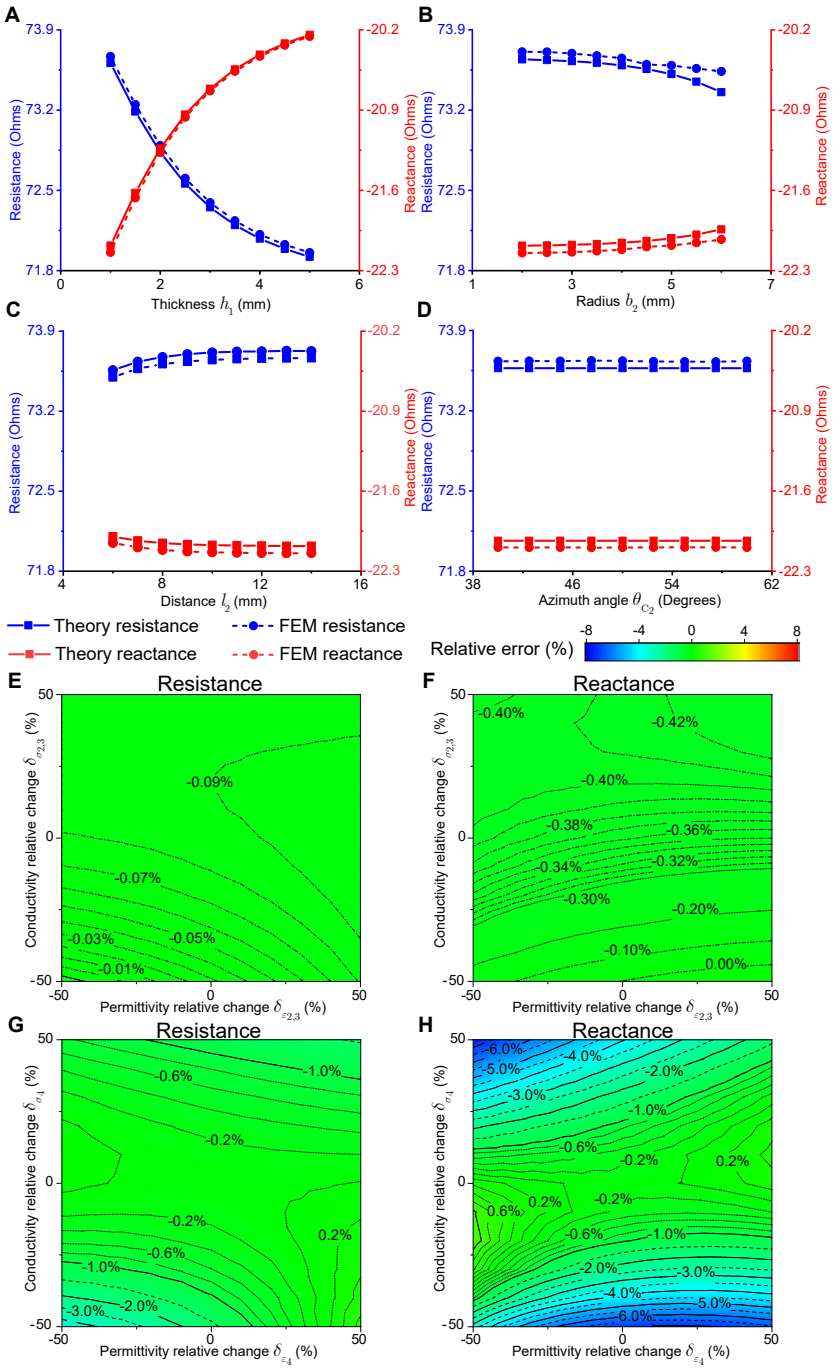

Figure 16. Analytical and FEM-simulated impedance results of case study 4 (see Figure 10 C and Figure 12 D). Theoretical (solid line) and FEM-simulated (dotted line) resistance and reactance with $h_1 = [1,5]$ mm, $l_{\{2,3\}} = 8$ mm, $b_{\{2,3\}} = 2$ mm, $\theta_{C_{\{2,3\}}} = 70^\circ$ (A); $b_2 = [2,6]$ mm, $b_3 = 4$ mm, $l_{\{2,3\}} = 10$ mm, $\theta_{C_{\{2,3\}}} = 45^\circ$ (B); $l_2 = [6,14]$ mm , $l_3 = 7$ mm, $h_1 = 1$ mm, $b_{\{2,3\}} = 3$ mm, $\theta_{C_{\{2,3\}}} = 45^\circ$ (C); $\theta_{C_2} = [40^\circ, 60^\circ]$, $\theta_{C_3} = 45^\circ$, $l_{\{2,3\}} = 7$ mm, $b_{\{2,3\}} = 3$ mm (D). Additional simulation setting parameters: $\sigma_1 = 1\,\mathrm{S\,m^{-1}}$, $\varepsilon_{r2} = 1 \times 10^5$ (dimensionless), $\sigma_2 = 1.1\,\mathrm{S\,m^{-1}}$, $\varepsilon_{r2} = 1.1 \times 10^5$ (dimensionless), $\sigma_3 = 0.9\,\mathrm{S\,m^{-1}}$, $\varepsilon_{r3} = 0.9 \times 10^5$ (dimensionless), $\sigma_4 = 0.95\,\mathrm{S\,m^{-1}}$, $\varepsilon_{r4} = 1.05 \times 10^5$ (dimensionless). Relative resistance and reactance errors changing the admittivity of domain $\Omega_{\{2,3\}}$ (i.e, $\delta_{\sigma_{2,3}} = \delta_{\sigma_2} = \delta_{\sigma_3}$, $\delta_{\varepsilon_{2,3}} = \delta_{\varepsilon_2} = \delta_{\varepsilon_3}$) (E, F) with $\sigma_4 = 1.1\,\mathrm{S\,m^{-1}}$, $\varepsilon_{r4} = 0.9 \times 10^5$ (dimensionless). Relative resistance and reactance errors changing the admittivity of domain Ω_4 (i.e, δ_{σ_4}, δ_{ε_4}) (G, H) with $\sigma_{\{2,3\}} = 1.1\,\mathrm{S\,m^{-1}}$, $\varepsilon_{\{r2,r3\}} = 0.9 \times 10^5$ (dimensionless). Additional simulation setting parameters: $\sigma_1 = 1\,\mathrm{S\,m^{-1}}$, $\varepsilon_{r2} = 1 \times 10^5$ (dimensionless), $h_1 = 2$ mm, $l_{\{2,3\}} = 8$ mm, $b_{\{2,3\}} = 3$ mm, $\theta_{C_{\{2,3\}}} = 45^\circ$.

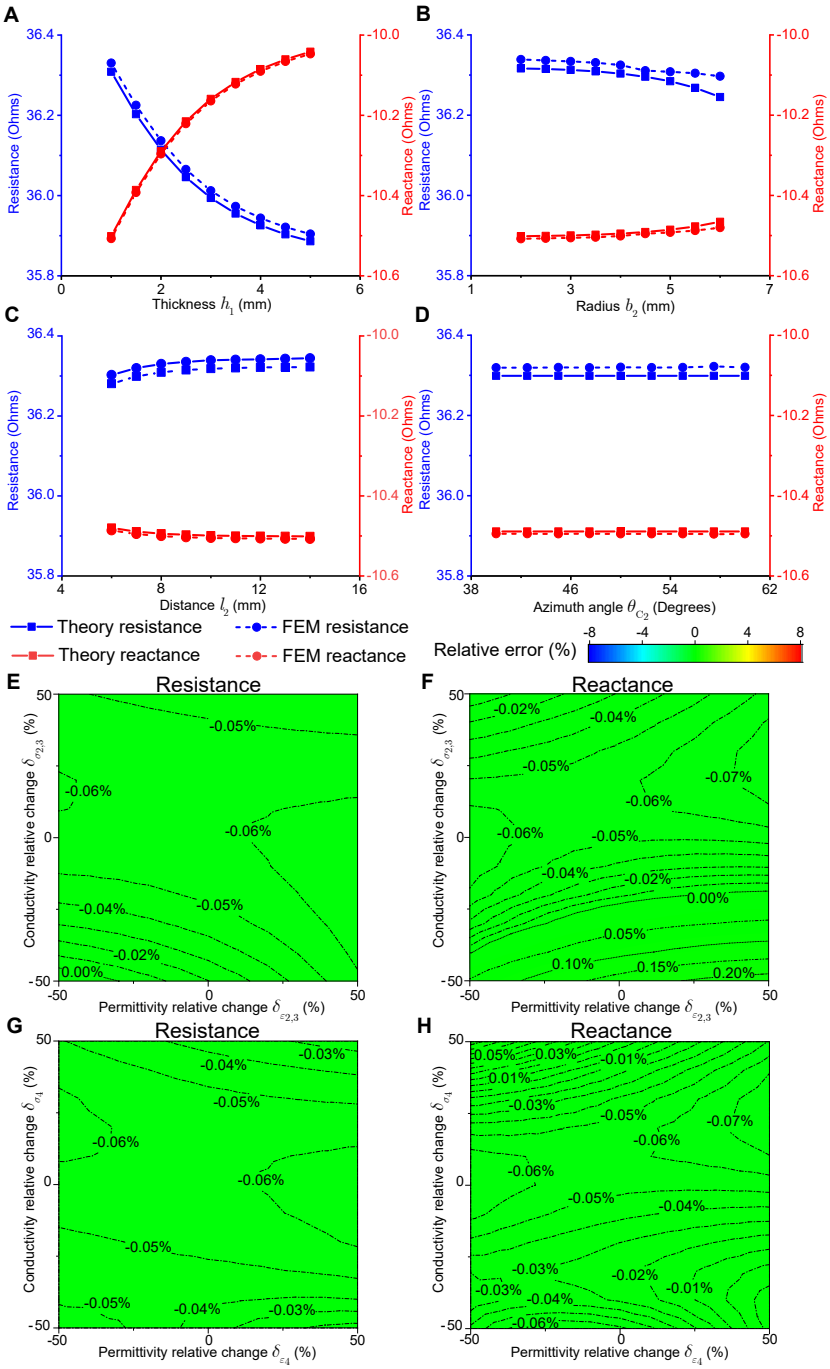

Figure 17. Analytical and FEM-simulated impedance results of case study 5 (see Figure 12 E). Theoretical (solid line) and FEM-simulated (dotted line) resistance and reactance with $h_1 = [1,5]$ mm, $l_{\{2,3\}} = 8$ mm, $b_{\{2,3\}} = 2$ mm, $\theta_{C_{\{2,3\}}} = 70^\circ$ (A); $b_2 = [2,6]$ mm, $b_3 = 4$ mm, $l_{\{2,3\}} = 10$ mm, $\theta_{C_{\{2,3\}}} = 45^\circ$ (B); $l_2 = [6,14]$ mm , $l_3 = 7$ mm, $h_1 = 1$ mm, $b_{\{2,3\}} = 3$ mm, $\theta_{C_{\{2,3\}}} = 45^\circ$ (C); $\theta_{C_2} = [40^\circ, 60^\circ]$, $\theta_{C_3} = 45^\circ$, $l_{\{2,3\}} = 7$ mm, $b_{\{2,3\}} = 3$ mm (D). Additional simulation setting parameters: $\sigma_1 = 1\,\mathrm{S\,m^{-1}}$, $\varepsilon_{r2} = 1 \times 10^5$ (dimensionless), $\sigma_2 = 1.1\,\mathrm{S\,m^{-1}}$, $\varepsilon_{r2} = 1.1 \times 10^5$ (dimensionless), $\sigma_3 = 0.9\,\mathrm{S\,m^{-1}}$, $\varepsilon_{r3} = 0.9 \times 10^5$ (dimensionless), $\sigma_4 = 0.95\,\mathrm{S\,m^{-1}}$, $\varepsilon_{r4} = 1.05 \times 10^5$ (dimensionless). Relative resistance and reactance errors changing the admittivity of domain $\Omega_{\{2,3\}}$ (i.e, $\delta_{\sigma_{2,3}} = \delta_{\sigma_2} = \delta_{\sigma_3}$, $\delta_{\varepsilon_{2,3}} = \delta_{\varepsilon_2} = \delta_{\varepsilon_3}$) (E, F) with $\sigma_4 = 1.1\,\mathrm{S\,m^{-1}}$, $\varepsilon_{r4} = 0.9 \times 10^5$ (dimensionless). Relative resistance and reactance errors changing the admittivity of domain Ω_4 (i.e, δ_{σ_4}, δ_{ε_4}) (G, H) with $\sigma_{\{2,3\}} = 1.1\,\mathrm{S\,m^{-1}}$, $\varepsilon_{\{r2,r3\}} = 0.9 \times 10^5$ (dimensionless). Additional simulation setting parameters: $\sigma_1 = 1\,\mathrm{S\,m^{-1}}$, $\varepsilon_{r2} = 1 \times 10^5$ (dimensionless), $h_1 = 2$ mm, $l_{\{2,3\}} = 8$ mm, $b_{\{2,3\}} = 3$ mm, $\theta_{C_{\{2,3\}}} = 45^\circ$.

properties of spherical volumes are $< 0.5\%$ for case study 4 (Figure 16 E, F) and $\leq 0.2\%$ for case study 5 (Figure 17 E, F). If we consider changes in the conductivity and relative permittivity properties of the two-layered tissues, then the maximum errors are $< 8\%$ for case study 4 (Figure 16 G, H) and $< 0.08\%$ for case study 5 (Figure 17 G, H). We note that case study 5 in full space has better model accuracy than half-space in case study 4.

9. Discussion

9.1. Nonhomogeneous multi-domain and isotropic framework in half and full space

This paper proposes a novel physics-driven framework for modeling electrical bioimpedance measurements of nonhomogeneous tissue considering both conductivity and relative permittivity properties of tissues along with their frequency dependence. Our theoretical framework can be used to model both surface and needle measurement of nonhomogeneous tissue with arbitrary shape considering *series*, *parallel*, and *series-parallel* circuit-like topologies. In these topologies, we first determine the electrical potential distribution within the model, the (approximated) apparent impedance and finally its sensitivity to changes in tissue electrical properties. For each topology, we confirm the usefulness of our framework performing numerical and FEM simulations considering up to 5 case studies. In summary, the simulation results reveal a maximum resistance and reactance error of $< 4\%$ and $< 8\%$, respectively.

9.2. Comparison to previous literature

Table 3. Review of nonhomogeneous theoretical studies published in the literature sorted by year of publication. Notation: $\sigma \in \mathbb{R}$, conductivity; $\rho \in \mathbb{R}$, resistivity; $\gamma \in \mathbb{C}$, admittivity; $\mathbb{R}^3_-$, half space; $\mathbb{R}^3$, full space; $Z \in \mathbb{C}$, impedance.

Authors	Electrical property	# domains	Model geometry	Current source	Model input	Model output	Impedance sensitivity	Application
(Alfano 1962)	Isotropic ρ	3, 4	Layered domain in $\mathbb{R}^3_-$	Implanted, point-like	Direct current	Apparent ρ	No	Geophysics
(Clark & Plonsey 1966)	Isotropic σ	2	Cylinder in $\mathbb{R}^3$	Nerve, cylindrical surface	Transmembrane current	Electrical potential	N.A.	Biophysics
(Clark & Plonsey 1968)	Isotropic σ	3	Nested cylinders in $\mathbb{R}^3$	Nerve, cylindrical surface	Transmembrane current	Electrical potential	N.A.	Biophysics
(Clark & Plonsey 1970)	Isotropic σ	3	Two cylinders in $\mathbb{R}^3$	Nerve, cylindrical surface	Transmembrane current	Electrical potential	N.A.	Biophysics
(Large 1971)	Isotropic ρ	2	Sphere in $\mathbb{R}^3_-$	Surface, point-like	Steady state current	Electrical potential	N.A.	Geophysics
(Merkel & Alexander 1971)	Isotropic ρ	2	Sphere in $\mathbb{R}^3_-$	Implanted, point-like	Steady state current	Apparent ρ	No	Geophysics
(Lee 1972)	Isotropic ρ	2	Two-dimensional media in $\mathbb{R}^3_-$	Surface, point-like	Steady state current	Apparent ρ	No	Geophysics
(Snyder & Merkel 1973)	Isotropic ρ	2, 3	Three-layered model and sphere in $\mathbb{R}^3_-$	Implanted, point-like	Steady state current	Electrical potential	N.A.	Geophysics
(Plonsey 1974)	Anisotropic σ	2	Cylinder in $\mathbb{R}^3$	N.A.	Electrical potential	Electrical potential	N.A.	Biophysics
(Lee 1975)	Isotropic σ	2, 3	Sphere, cylinder in two-layered volume	Surface, point-like	Steady state current	Electrical potential	N.A.	Geophysics
(Snyder 1976)	Isotropic σ	2	Two-dimensional media	Surface, point-like	Direct current	Electrical potential	N.A.	Geophysics
(Singh 1976)	Isotropic ρ	2	Sphere in $\mathbb{R}^3_-$	Surface, point-like	Direct current	Apparent ρ	No	Geophysics
(Plonsey 1977)	Isotropic σ	2	Arbitrary surface in $\mathbb{R}^3$	N.A.	Electrical potential	Electrical potential	N.A.	Biophysics
(Greco & Clark 1977)	Isotropic σ	2	Cylinder in $\mathbb{R}^3$	N.A.	Electrical potential	Electrical potential	N.A.	Biophysics
(Stegeman et al. 1979)	Anisotropic σ	3	Nest cylinders in $\mathbb{R}^3_-$	Nerve, cylindrical surface	Transmembrane current	Electrical potential	N.A.	Biophysics
(Robillard & Poussart 1979)	Isotropic ρ	2	Two-layered volume in $\mathbb{R}^3$	Implanted, point-like	Alternating current	Apparent ρ	No	Biophysics
(Lytle 1982)	Isotropic ρ	2	Sphere in $\mathbb{R}^3$	Implanted, point-like	Alternating current	Electrical potential	N.A.	Geophysics
(Wilson et al. 1985)	Anisotropic σ	4	Nested cylinders in $\mathbb{R}^3$	N.A.	Electrical potential	Electrical potential	N.A.	Biophysics
(Ganapathy & Clark 1987)	Isotropic σ	2	Cylinders in $\mathbb{R}^3$	Nerve, cylindrical surface	Transmembrane current	Electrical potential	N.A.	Biophysics
(Ganapathy et al. 1987)	Anisotropic σ	3	Nested cylinders in $\mathbb{R}^3$	N.A.	Electrical potential	Electrical potential	N.A.	Biophysics
(Altman & Plonsey 1988) (Altman & Plonsey 1990)	Anisotropic σ	2	Cylinder in $\mathbb{R}^3$	Implanted, point-like	Transmembrane current	Electrical potential	N.A.	Biophysics
(Trayanova et al. 1993)	Anisotropic σ	2	Sphere in $\mathbb{R}^3$	Cardiac, spherical shell	Transmembrane current	Electrical potential	N.A.	Biophysics
(Roth 1997)	Anisotropic σ	2	Two-dimensional media in $\mathbb{R}^3$	Implanted, point-like	Steady state current	Electrical potential	N.A.	Biophysics
(Vickery & Hobbs 2002)	Isotropic ρ	2	Cylinder in $\mathbb{R}^3_-$	Surface, point-like	Steady state current	Apparent ρ	No	Geophysics
(Joshi & Song 2010)	Isotropic γ	3	Nested Cylinders in $\mathbb{R}^3$	Implanted, point-like	Pulsed current	Electrical potential	N.A.	Biophysics
(Ness et al. 2015)	Anisotropic σ	2	Cylinder in Two-layered volume in $\mathbb{R}^3$	Implanted, point-like	Alternating current	Electrical potential	N.A.	Biophysics
(Schwartz & Sadleir 2015) (Schwartz et al. 2016)	Isotropic ρ	2	Sphere in $\mathbb{R}^3$	Implanted, point-like	Alternating current	Electrical potential	N.A.	Biophysics
(Neu 2016)	Isotropic σ	2	Cylinder in $\mathbb{R}^3$	Implanted, point-like	Stimulating current	Electrical potential	N.A.	Biophysics
This study	Isotropic γ	≥ 2	Arbitrary *series*, *parallel*, *series-parallel* in $\mathbb{R}^3_-$ and $\mathbb{R}^3$	Surface/Implanted, point-like	Alternating current	Electrical potential, apparent Z	Yes	Biophysics

To put the novelty and contribution of our work in context, we provide in Table 3 a review of studies published in the literature where the authors developed theoretical frameworks for modeling nonhomogeneous media. Table 3 shows that a large number of studies were developed to determine the electrical potential measured caused by transmembrane current, e.g, due to membrane depolarization (Clark & Plonsey 1966, Clark & Plonsey 1968, Clark & Plonsey 1970). These studies focused on modeling the propagation of the electrical potential generated for example in a cylindrical nerve cell, and propagated through the surrounding bulk of (anisotropic) muscle, subcutaneous fat and skin and then finally recorded with a distant electrode from the source (Altman & Plonsey 1988, Altman & Plonsey 1990). These studies were essential to understand the low-pass frequency filtering effects affecting the morphology of extracellular potentials introduced by intermediate tissue between the source of current and a distant voltage recording electrode. Subsequently, the number of domains considered is not more than 4 with cylindrical geometry in order to model the anatomical shape of a limb for example. Although not related to physiological measurement, a review of the literature would be incomplete without including nonhomogeneous models developed in the field of geophysical surveying for soil determination. In this particular application, models developed were primarily based on soil resistivity for applications including ore detection (Lytle 1982).

It is also worth noting that in most studies, regardless of the directionality of electrical properties, the only conduction effect considered is purely ohmic through the resistivity (or its inverse, the conductivity, if the relative permittivity is ignored). To the best of the authors' knowledge, we are only aware of one previous study where the authors considered both the conductivity and the relative permittivity (i.e., the admittivity) in the propagation of the electrical potential in a cylindrical domain (Joshi & Song 2010), however, our framework is more general in the sense that it can model any parameterizable geometry. By considering the admittivity, we not only provide an approximated analytical expression of the electric potential but also an approximate analytical expression for the apparent impedance including the imaginary part (i.e., the reactance). Compared to existing literature, our framework is general enough to model an arbitrary number of domains. This may help to get insight not currently available in emerging bioimpedance applications in which there is not a cylindrical tissue geometry, for example, a localized bioimpedance measure of pulsatile blood flow on the wrist (Kusche et al. 2018) or neck (Shen et al. 2019) for the next generation of wearable devices.

Unlike studies where the authors solved the Poission' equation considering a specific nonhomogeneous geometry (Lee 1975, Altman & Plonsey 1990), the gist of our approach to solve a generic nonhomogeneous topology lies in using an iterative approximation strategy. In doing so, we were able to obtain a general bioimpedance expression for nonhomogeneous tissue separating the contribution of the domains' electrical property, the electrodes geometry, and domain geometry. This allowed us to provide an analytical expression for the sensitivity to electrical changes in individual domains within the nonhomogeneous tissue, which has not been done before. This is especially relevant because it allows the user to predict the impedance change due to a change in internal conductivity in one of the domains within the nonhomogeneous tissue. Finally, our modeling approach allowed us to interpret

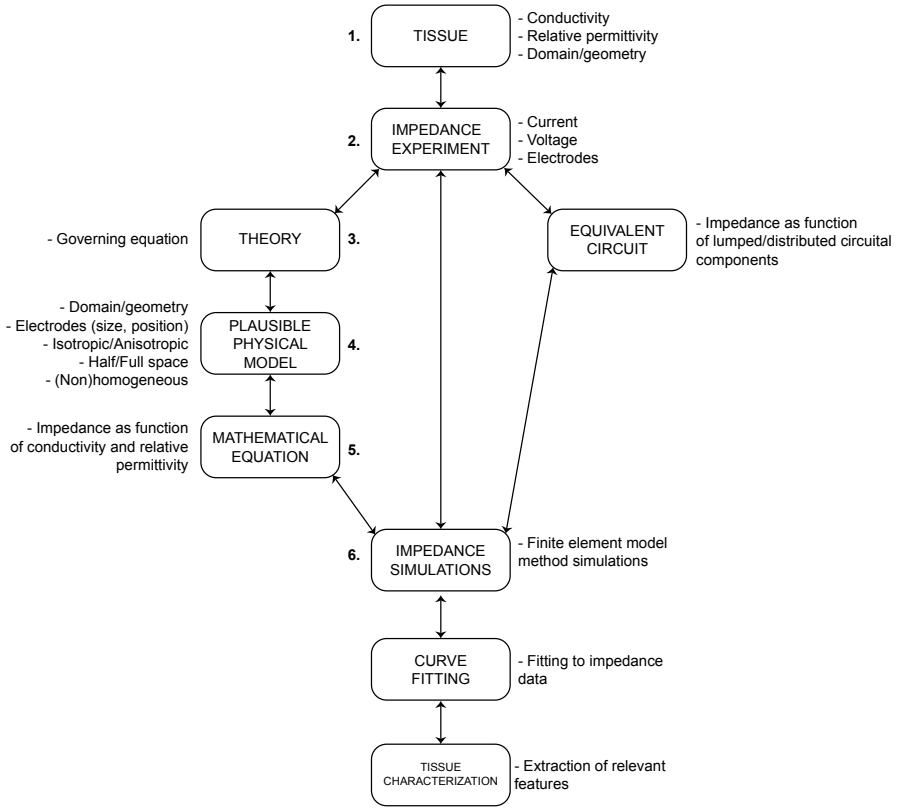

Figure 18. Flow diagram showing the approaches available for model bioimpedance. In this work we have followed steps 1 to 6.

nonhomogeneous tissue with electrical circuit equivalents such as series, parallel and series-parallel, introducing a novel theoretical concept that also has never been applied before and which raises further questions, discussed below.

9.3. Comparison to other bioimpedance modeling approaches

There exist three modeling approaches to interpret nonhomogeneous bioimpedance illustrated in Figure 18: physics-driven models, computational models and equivalent electrical circuit models. Unlike FEM only and circuit-based approaches, the theoretical approach presented provides a *general* and structured framework to describe macroscopically nonhomogeneous bioimpedance measurement directly relating electrodes, domain and tissue electrical properties. As any theoretical study, assumptions are necessary to solve the governing equations analytically such as considering the domain (semi-)infinite. FEM modeling approaches would be helpful to further investigate the accuracy of our theoretical predictions when these assumptions are not met, for example, modeling a finite-shape domain. Modeling bioimpedance using equivalent circuits is, compared to our approach and FEM methods, fundamentally different. In this case, data is described by empirical circuits which is valuable for simplifying the complex nature originating bioimpedance data using a circuital parameter of interest.

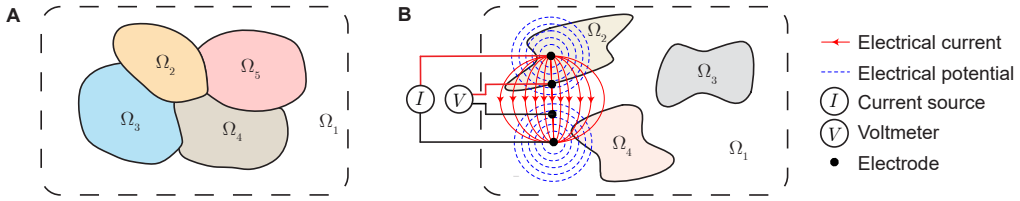

Figure 19. (A) Schematic representing the nonhomogeneous tissue with intersecting domains Ω_i, $i \in \{1, \cdots, 5\}$. (B) Schematic illustrating a nonhomogeneous impedance measurement with current and voltage electrodes in different domains. The outer two electrodes are the high (source) and low (sink) current electrodes, whereas the inner electrodes are the high and low potential recording electrodes.

9.4. Limitations

This study has important limitations that are worth highlighting. First, modeling nonhomogeneous tissue with *series*, *parallel* and *series-parallel* circuit-like topologies is a simplification that does not describe all possible nonhomogeneities. Albeit general, it cannot model a nonhomogeneous tissue consisting of the intersection between different domains shown in Figure 19 A. Second, the electrodes are assumed to be in contact with just one (i.e., the same) domain within the nonhomogeneous tissue. Further research is necessary to extend the framework to model an arbitrary positioning of the electrodes in different domains with different admittivity properties or even on the boundary between domains (Figure 19 B). Third, the framework is developed assuming the electrodes are placed on a planar surface. This might not be possible to achieve in practice, especially in curved surfaces such as the wrist. Fourth, we considered all domains to have isotropic admittivity properties. In tissues like skeletal muscle, the admittivity has different values along and perpendicular to the muscle fiber, a concept known as electrical anisotropy (Kwon, Guasch, Nagy, Rutkove & Sanchez 2019). Fifth, the framework was developed considering point-like source and electrodes, a more realistic approach would required to consider their finite-size.

9.5. Future directions

We foresee three different future directions stemming from the current work:

(i) Extend the forward framework to model a nonhomogeneous tissue with intersecting domains, arbitrary electrode positioning, anisotropic electrical properties, and finite-size electrodes geometry.

(ii) Develop inverse models to estimate the electrical properties from nonhomogeneous tissue bioimpedance measurements.

(iii) Apply the framework to model non-invasive and penetrating needle bioimpedance measurements of nonhomogeneous tissues. Two examples are surface electrical impedance myography applications to model the effect of intermediate tissues such as the skin and subcutaneous fat tissues affecting muscle readings, and wearable impedance cardiography measurements to disentangle the source of electrical conductivity

originating changes in thoracic bioimpedance measurements.

10. Conclusions

Our work provides new scientific insight to model bioimpedance measurements of nonhomogeneous tissues. This framework might find use for interpreting bioimpedance measurements in multi-domain nonhomogeneous tissues with arbitrary boundary surfaces in half and full space considering both the conductivity and the relative permittivity properties. Simple analytical expressions validated by FEM simulations are also provided for 5 particular case studies considering spherical and multi-layer tissues. Ultimately, this knowledge will help to aid the development of more accurate bioimpedance devices and shed light on the interpretation of bioimpedance results in a multitude of health-related moniitoring applications.

Conflict of interest statement

Dr. Sanchez has equity and serves a consultant and scientific advisor to Haystack^{Dx}, Inc. and IONIQ Sciences, Inc.. He also serves as scientific advisor to B-Secur, Ltd. Dr. Sanchez serves as a consultant to Myolex, Inc., Impedimed, Inc., Texas Instruments, Inc., Happy Health, Inc., companies that develop impedance related technology for consumer, research and clinical use. Haystack^{Dx} and Myolex have an option to license patented impedance technology of which Dr. Sanchez is named as an inventor. Impedimed has patented impedance technology of which Dr. Sanchez is named an inventor. This study did not employ any relevant company technology.

Acknowledgments

This work was funded by the China Scholarship Council grant 201906020024 (XL) and National Institutes of Health grant R41 NS112029-01A1 (BS).

11. References

Alfano L 1962 *Geophysical Prospecting* **10**(3), 290–303.
Altman K & Plonsey R 1988 *Medical and Biological Engineering and Computing* **26**(5), 466–475.
Altman K W & Plonsey R 1990 *IEEE transactions on biomedical engineering* **37**(7), 688–698.
Bachasson D, Ayaz A C, Mosso J, Canal A, Boisserie J M, Araujo E C, Benveniste O, Reyngoudt H, Marty B, Carlier P G et al. 2021 *Journal of Cachexia, Sarcopenia and Muscle* **12**(1), 39–51.
Clark J & Plonsey R 1966 *Biophysical journal* **6**(1), 95–112.
Clark J & Plonsey R 1968 *Biophysical journal* **8**(7), 842.
Clark J W & Plonsey R 1970 *Biophysical journal* **10**(10), 937–957.
Cohl H S & Tohline J E 1999 *The astrophysical journal* **527**(1), 86.
Cumming K, Hoyle G, Hutchison J & Soiza R L 2014 *The journal of nutrition, health & aging* **18**(8), 744–750.
Ganapathy N & Clark J W 1987 *Biophysical journal* **52**(5), 749–761.
Ganapathy N, Clark J W & Wilson O 1987 *Mathematical biosciences* **83**(1), 61–96.

Geselowitz D B 1971 *IEEE Transactions on Bio-Medical Engineering* **18**(1), 38–41.

Greco E C & Clark J W 1977 *IEEE Transactions on Biomedical Engineering* (1), 18–23.

Grimnes S & Martinsen O G 2011 *Bioimpedance and bioelectricity basics* Academic press.

Haas V, Riedl A, Hofmann T, Nischan A, Burghardt R, Boschmann M & Klapp B 2012 *European Eating Disorders Review* **20**(5), 400–405.

Hong Y T, Yun J, Lee J H & Hong K H 2020 *Auris Nasus Larynx* .

Ibrahim F, Taib M N, Abas W A B W, Guan C C & Sulaiman S 2005 *IEEE Transactions on Instrumentation and Measurement* **54**(1), 237–244.

Joshi R P & Song J 2010 *IEEE transactions on plasma science* **38**(10), 2894–2900.

Kusche R, Klimach P & Ryschka M 2018 *IEEE transactions on biomedical circuits and systems* **12**(3), 614–622.

Kwon H, Guasch M, Nagy J, Rutkove S & Sanchez B 2019 *Scientific reports* **9**(1), 1–16.

Kwon H, Malik W Q, Rutkove S B & Sanchez B 2019 *IEEE Transactions on Biomedical Engineering* **66**(2), 354–364.

Large D B 1971 *GEOPHYSICS* **36**(4), 763–767.

Lee T 1972 *Geophysical Prospecting* **20**(4), 847–859.

Lee T 1975 *Geophysical Journal International* **42**(1), 81–95.

Lorenzo M F, Bhonsle S, Arena C B & Davalos R V 2020 *IEEE Transactions on Biomedical Engineering* .

Lytle R J 1982 *IEEE Transactions on Geoscience and Remote Sensing* (4), 493–499.

Maxwell J C 1873 *A treatise on electricity and magnetism* Oxford: Clarendon Press.

Merkel R & Alexander S 1971 *Geophysical Prospecting* **19**(4), 640–651.

Ness T V, Chintaluri C, Potworowski J, Łęski S, Głąbska H, Wójcik D K & Einevoll G T 2015 *Neuroinformatics* **13**(4), 403–426.

Neu W K 2016 *Medical & biological engineering & computing* **54**(11), 1719–1725.

Parke R L, Bloch A & McGuinness S P 2015 *Respiratory Care* **60**(10), 1397–1403.

Plonsey R 1974 *IEEE transactions on biomedical engineering* (5), 371–381.

Plonsey R 1977 *Proceedings of the IEEE* **65**(5), 601–611.

Robillard P N & Poussart D 1979 *IEEE Transactions on Biomedical Engineering* (8), 465–470.

Roth B J 1997 *Physical Review E* **55**(2), 1819.

Rutkove S B & Sanchez B 2018 *Cold Spring Harbor perspectives in medicine* p. a034405.

Sanchez B, Martinsen O G, Freeborn T J & Furse C M 2020 *Clinical Neurophysiology* .

Schwan H & Foster K 1989 *Crit. Rev. Biomed. Eng* **17**, 25–104.

Schwartz B L, Chauhan M & Sadleir R J 2016 *The Journal of Mathematical Neuroscience* **6**(1), 1–20.

Schwartz B L & Sadleir R J 2015 *in* '2015 37th Annual International Conference of the IEEE Engineering in Medicine and Biology Society (EMBC)' IEEE pp. 2299–2302.

Shen H, Li S, Wang Y & Qin K R 2019 *Medical & biological engineering & computing* **57**(2), 441–451.

Singh S K 1976 *Computers & Geosciences* **1**(4), 241–245.

Snyder D D 1976 *Geophysics* **41**(5), 997–1015.

Snyder D D & Merkel R M 1973 *Geophysics* **38**(3), 513–529.

Stegeman D, De Weerd J & Eijkman E 1979 *Biological cybernetics* **33**(2), 97–111.

Trayanova N A, Roth B J & Malden L J 1993 *IEEE transactions on biomedical engineering* **40**(9), 899–908.

Vickery A C & Hobbs B A 2002 *Geophysical Prospecting* **50**(1), 1–13.

Wazwaz A M 2007 *Computers & Mathematics with Applications* **54**(7-8), 926–932.

Wilson O B, Clark J W, Ganapathy N & Harman T 1985 *IEEE transactions on biomedical engineering* (12), 1032–1041.

Zamani M, Rezaeiyan Y, Shoaei O & Serdijn W A 2018 *IEEE transactions on biomedical circuits and systems* **12**(1), 211–221.

Supplementary information for "A framework for modeling bioimpedance measurements in nonhomogeneous tissues: a theoretical and simulation study"

1 Lemma 1.

If $\partial\Omega_i$ is a spherical surface centered at C_i with radius b_i in $\mathbb{R}^3$, Q_i is an arbitrary point on $\partial\Omega_i$, $\mathbf{n}_i$ is the outward normal vector at Q_i, S and E are arbitrary points outside the sphere as shown in Figure A1, then

$$\begin{aligned} -\frac{1}{2\pi}\iint_{\partial\Omega_i}\frac{\partial R_{\mathrm{SQ}_i}(\mathbf{r}_{\mathrm{Q}_i})}{\partial\mathbf{n}_i}\cdot\mathbf{n}_i\frac{\mathrm{d}(\partial\Omega_i)}{R^2_{\mathrm{SQ}_i}(\mathbf{r}_{\mathrm{Q}_i})R_{\mathrm{EQ}_i}(\mathbf{r}_{\mathrm{Q}_i})} \\ =\frac{1}{b_i}\sum_{n=0}^{\infty}\frac{2n}{2n+1}\left(\frac{b_i^2}{R_{\mathrm{EC}_i}R_{\mathrm{SC}_i}}\right)^{n+1}P_n(\cos\theta_i). \end{aligned} \tag{A1}$$

Proof. To calculate the surface integrals in (A1) we build an auxiliary model of charged spherical shell in vacuum that allows us to find the solution indirectly. Let's start establishing a spherical coordinates in $\mathbb{R}^3$ originated at the center C_i of the spherical surface $\partial\Omega_i$ (see Figure A1). The position $\mathbf{r} := (r,\theta,\varphi)$ is an arbitrary defined in spherical coordinates. For convenience, we consider S with coordinates $\mathbf{r}_{\mathrm{S}} := (R_{\mathrm{SC}_i},0,0)$ on the z-axis, while E is defined with coordinates $\mathbf{r}_{\mathrm{E}} := (R_{\mathrm{EC}_i},\theta_i,0)$, while Q_i with coordinates $\mathbf{r}_{\mathrm{Q}_i} := (b_i,\theta_{\mathrm{Q}_i},\varphi_{\mathrm{Q}_i})$ is an arbitrary point on $\partial\Omega_i$. R_{SC_i} is the distance between S and C_i; R_{EC_i} is the distance between E and C_i; R_{SQ_i} is the distance between S and Q_i; R_{EQ_i} is the distance between E and Q_i; θ_i is the angle between line segment $|SC_i|$ and $|EC_i|$; θ_{Q_i} is the angle between line segment $|Q_iC_i|$ and $|SC_i|$. Next, we introduce a charge density function $q(\mathbf{r}_{\mathrm{Q}_i})\in\mathbb{R}$ (C m^{-2}) on the spherical surface $\partial\Omega_i$, defined as

$$q(\mathbf{r}_{\mathrm{Q}_i}) := \frac{\partial R_{\mathrm{SQ}_i}(\mathbf{r}_{\mathrm{Q}_i})}{\partial\mathbf{n}_i}\cdot\mathbf{n}_i\frac{1}{R^2_{\mathrm{SQ}_i}(\mathbf{r}_{\mathrm{Q}_i})}.$$

Then the potential distribution $U(\mathbf{r})$ caused by Q_i can be expressed as

$$U(\mathbf{r}) = \frac{1}{4\pi\varepsilon_0}\iint_{\partial\Omega_i}\frac{\partial R_{\mathrm{SQ}_i}(\mathbf{r}_{\mathrm{Q}_i})}{\partial\mathbf{n}_i}\cdot\mathbf{n}_i\frac{1}{R^2_{\mathrm{SQ}_i}(\mathbf{r}_{\mathrm{Q}_i})}\frac{\mathrm{d}(\partial\Omega_i)}{\left|\mathbf{r}-\mathbf{r}_{\mathrm{Q}_i}\right|}. \tag{A2}$$

According to the axial symmetry, U has no dependence on the azimuthal angle φ. Then applying separation of variables to Poission's equation, the general solution for potential distribution $U(\mathbf{r})$ in spherical coordinates satisfies that

$$U(\mathbf{r}) = \sum_{n=0}^{\infty}\left(A_n r^n + \frac{B_n}{r^{n+1}}\right)P_n(\cos\theta), \tag{A3}$$

where A_n and B_n are a series of constants and $P_n(x)$ are Legendre polynomials.

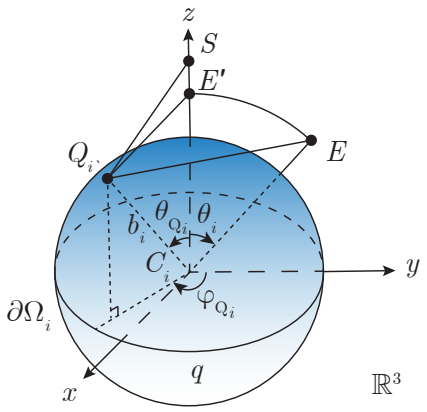

Figure A1: Auxiliary model of charged spherical shell in vacuum. A nonuniform charged spherical shell $\partial\Omega_i$ is centered at the origin of spherical coordinates (r,θ,φ) in infinity vacuum $\mathbb{R}^3$with b_i the radius of $\partial\Omega_i$. The position Q_i has coordinates $\mathbf{r}_{\mathrm{Q}_i} := (b_i,\theta_{\mathrm{Q}_i},\varphi_{\mathrm{Q}_i})$ on $\partial\Omega_i$. The charge density $q(\mathbf{r}_{\mathrm{Q}_i})$ is distributed on surface $\partial\Omega_i$. The position S, E and E' have coordinates $\mathbf{r}_{\mathrm{S}} := (R_{\mathrm{SC}_i},0,0)$, $\mathbf{r}_{\mathrm{E}} := (R_{\mathrm{EC}_i},\theta_i,0)$ and $\mathbf{r}_{\mathrm{E}'} := (R_{\mathrm{EC}_i},0,0)$ outside the sphere, which satisfy $|EC_i| = |E'C|$ and S, E' are on z-axis. The angle θ_i is defined between line segment $|SC_i|$ and $|EC_i|$; θ_{Q_i} is the angle between line segment $|SC_i|$ and $|Q_iC_i|$.

In this model, an auxiliary point E' with coordinates $\mathbf{r}_{\mathrm{E}} := (R_{\mathrm{EC}_i},0,0)$ is introduced to solve the surface integral (A2) indirectly, which satisfy $|E'C_i| = |EC_i|$ and E' is on z-axis. From (A3), the potential at E' can be written as

$$U(\mathbf{r}_{\mathrm{E}'}) = \sum_{n=0}^{\infty}\left(A_n R_{\mathrm{EC}_i}^n + \frac{B_n}{R_{\mathrm{EC}_i}^{n+1}}\right). \tag{A4}$$

From (A2), $V(\mathbf{r}_{\mathrm{E}'})$ can also be expressed as

$$U(\mathbf{r}_{\mathrm{E}'}) = \frac{1}{4\pi\varepsilon_0}\int_{-\pi}^{\pi}\int_0^{\pi}\frac{\partial R_{\mathrm{SQ}_i}(\mathbf{r}_{\mathrm{Q}_i})}{\partial b_i}\frac{b_i^2\sin\theta_{\mathrm{Q}_i}\mathrm{d}\theta_{\mathrm{Q}_i}\mathrm{d}\varphi_{\mathrm{Q}_i}}{R_{\mathrm{SQ}_i}^2(\mathbf{r}_{\mathrm{Q}_i})R_{\mathrm{Q}_i\mathrm{E}'}(\mathbf{r}_{\mathrm{Q}_i})}, \tag{A5}$$

where

$$R_{\mathrm{SQ}_i}(\mathbf{r}_{\mathrm{Q}_i}) = \sqrt{R_{\mathrm{SC}_i}^2 + b_i^2 - 2b_iR_{\mathrm{SC}_i}\cos\theta_{\mathrm{Q}_i}}$$

and

$$R_{\mathrm{Q}_i\mathrm{E}'}(\mathbf{r}_{\mathrm{Q}_i}) = \sqrt{R_{\mathrm{EC}_i}^2 + b_i^2 - 2b_iR_{\mathrm{EC}_i}\cos\theta_{\mathrm{Q}_i}}.$$

Equation (A5) can be further simplified as

$$U(\mathbf{r}_{\mathrm{E}'}) = \frac{1}{4\varepsilon_0}\left[\frac{2b_i}{b_i^2 - R_{\mathrm{EC}_i}R_{\mathrm{SC}_i}} + \frac{1}{\sqrt{R_{\mathrm{EC}_i}R_{\mathrm{SC}_i}}}\ln\left(\frac{\sqrt{R_{\mathrm{EC}_i}R_{\mathrm{SC}_i}}+b_i}{\sqrt{R_{\mathrm{EC}_i}R_{\mathrm{SC}_i}}-b_i}\right)\right]. \tag{A6}$$

From the geometry of the model, we have that $\frac{b_i}{\sqrt{R_{\mathrm{EC}_i}R_{\mathrm{SC}_i}}} < 1$. According to Taylor series we have

$$\begin{cases} \ln\left(\frac{\sqrt{R_{\mathrm{EC}_i}R_{\mathrm{SC}_i}}+b_i}{\sqrt{R_{\mathrm{EC}_i}R_{\mathrm{SC}_i}}-b_i}\right) & = \sum_{n=1}^{\infty}\frac{1}{n}\frac{b_i^n}{R_{\mathrm{EC}_i}^{\frac{n}{2}}R_{\mathrm{SC}_i}^{\frac{n}{2}}} + \sum_{n=1}^{\infty}\frac{(-1)^{n+1}}{n}\frac{b_i^n}{R_{\mathrm{EC}_i}^{\frac{n}{2}}R_{\mathrm{SC}_i}^{\frac{n}{2}}} \\ \frac{2b_i}{b_i^2-R_{\mathrm{EC}_i}R_{\mathrm{SC}_i}} & = -\frac{2b_i}{R_{\mathrm{EC}_i}R_{\mathrm{SC}_i}}\sum_{n=0}^{\infty}\frac{b_i^{2n}}{R_{\mathrm{EC}_i}^{n}R_{\mathrm{SC}_i}^{n}} \end{cases} \tag{A7}$$

Substituting (A7) into (A6) gives

$$U(\mathbf{r}_{\mathrm{E}'}) = -\frac{1}{b_i\varepsilon_0}\sum_{n=0}^{\infty}\frac{n}{2n+1}\left(\frac{b_i^2}{R_{\mathrm{EC}_i}R_{\mathrm{SC}_i}}\right)^{n+1}. \tag{A8}$$

Comparing (A8) and (A4), we have

$$\begin{cases} A_n = 0 \\ B_n = -\frac{1}{\varepsilon_0}\frac{nb_i^{2n+1}}{(2n+1)R_{\mathrm{SC}_i}^{n+1}}. \end{cases} \tag{A9}$$

Substituting (A9) to (A3) gives

$$U(\mathbf{r}) = -\frac{1}{\varepsilon_0}\sum_{n=0}^{\infty}\frac{nb_i^{2n+1}}{(2n+1)R_{\mathrm{SC}_i}^{n+1}}\frac{1}{r^{n+1}}P_n(\cos\theta). \tag{A10}$$

Then the potential at E is

$$U(\mathbf{r}_{\mathrm{E}}) = -\frac{1}{b_i\varepsilon_0}\sum_{n=0}^{\infty}\frac{n}{2n+1}\left(\frac{b_i^2}{R_{\mathrm{EC}_i}R_{\mathrm{SC}_i}}\right)^{n+1}P_n(\cos\theta_i). \tag{A11}$$

According to (A2), $U(\mathbf{r}_{\mathrm{E}})$ can also be written as

$$U(\mathbf{r}_{\mathrm{E}}) = \frac{1}{4\pi\varepsilon_0}\iint_{\partial\Omega_i}\frac{\partial R_{\mathrm{SQ}_i}(\mathbf{r}_{\mathrm{Q}_i})}{\partial\mathbf{n}_i}\cdot\mathbf{n}_i\frac{\mathrm{d}(\partial\Omega_i)}{R_{\mathrm{SQ}_i}^2(\mathbf{r}_{\mathrm{Q}_i})R_{\mathrm{EQ}_i}(\mathbf{r}_{\mathrm{Q}_i})}. \tag{A12}$$

One can find (A1) equating the right hand sides of (A11) and (A12). □

2 Lemma 2.

If $\partial\Omega_i$ is an infinity plane in $\mathbb{R}^3$, Q_i is an arbitrary point on $\partial\Omega_i$ and S, E are arbitrary points share the same distance N_i to plane $\partial\Omega_i$ as shown in Figure B1, then

$$-\frac{1}{2\pi}\iint_{\partial\Omega_i}\frac{\partial R_{\mathrm{SQ}_i}(\mathbf{r}_{\mathrm{Q}_i})}{\partial\mathbf{n}_i}\cdot\mathbf{n}_i\frac{\mathrm{d}(\partial\Omega_i)}{R_{\mathrm{SQ}_i}^2(\mathbf{r}_{\mathrm{Q}_i})R_{\mathrm{EQ}_i}(\mathbf{r}_{\mathrm{Q}_i})} = \frac{1}{\sqrt{R_{\mathrm{SE}}^2+4N_i^2}}. \tag{B1}$$

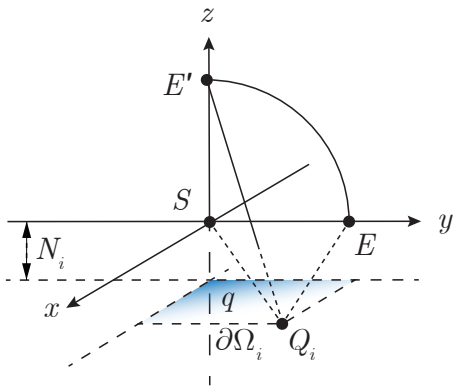

Figure B1: Auxiliary model of charged plane $\partial\Omega_i : z = -N_i$ in vacuum. The position Q_i has coordinates $\mathbf{r}_{\mathrm{Q}_i} := (x, y, -N_i)$ is an arbitrary point on the plane. The charge density $q(\mathbf{r}_{\mathrm{Q}_i})$ is distributed on $\partial\Omega_i$. Positions S, E and E' have coordinates $\mathbf{r}_{\mathrm{S}} := (0,0,0)$, $\mathbf{r}_{\mathrm{E}} := (0, R_{\mathrm{SE}}, 0)$ and $\mathbf{r}_{\mathrm{E}'} := (0,0,R_{\mathrm{SE}})$ in the vacuum, which satisfy the line segments $|ES| = |E'S|$.

Proof. We follow a similar procedure as we did in Lemma 1. First, we establish a Cartesian coordinates (x,y,z) in $\mathbb{R}^3$ with origin S at $\mathbf{r}_{\mathrm{S}} := (0,0,0)$. We then place E at $\mathbf{r}_{\mathrm{E}} := (0, R_{\mathrm{SE}}, 0)$ on the y-axis and $\partial\Omega_i$ as the normal plane of z-axis. The position Q_i is defined with coordinates $\mathbf{r}_{\mathrm{Q}_i} := (x, y, -N_i)$ on the plane $\partial\Omega_i : z = -N_i$. R_{SE} is the distance between S and E. Next, we introducing the same charge density distribution function $q(\mathbf{r}_{\mathrm{Q}_i})$ on the plane $\partial\Omega_i$ as in Lemma.1. According to (A2), $U(\mathbf{r}_{\mathrm{E}'})$ can be expressed as

$$U(\mathbf{r}_{\mathrm{E}'}) = \frac{1}{4\pi\varepsilon_0} \int_{-\infty}^{\infty}\int_{-\infty}^{\infty} -\frac{\partial R_{\mathrm{SQ}_i}(\mathbf{r}_{\mathrm{Q}_i})}{\partial N_i} \frac{\mathrm{d}x\mathrm{d}y}{R^2_{\mathrm{SQ}_i}(\mathbf{r}_{\mathrm{Q}_i}) R_{\mathrm{Q}_i\mathrm{E}'}(\mathbf{r}_{\mathrm{Q}_i})}, \tag{B2}$$

where

$$R_{\mathrm{SQ}_i}(\mathbf{r}_{\mathrm{Q}_i}) = \sqrt{x^2 + y^2 + N_i^2}$$

and

$$R_{\mathrm{Q}_i\mathrm{E}'}(\mathbf{r}_{\mathrm{Q}_i}) = \sqrt{x^2 + y^2 + (R_{\mathrm{SE}} + N_i)^2}.$$

Then, (B2) can be simplified as

$$U(\mathbf{r}_{\mathrm{E}'}) = -\frac{1}{2\varepsilon_0} \frac{1}{2N_i + R_{\mathrm{SE}}}. \tag{B3}$$

Equation (B3) can be rewritten using Taylor series as

$$U(\mathbf{r}_{\mathrm{E}'}) = \begin{cases} -\frac{1}{2\varepsilon_0} \sum_{n=0}^{\infty} \frac{(-1)^n 2^n N_i^n}{R_{\mathrm{SE}}^{n+1}} & \text{if } 2N_i < R_{\mathrm{SE}} \\ -\frac{1}{2\varepsilon_0} \sum_{n=0}^{\infty} \frac{(-1)^n R_{\mathrm{SE}}^n}{2^{n+1} N_i^{n+1}} & \text{if } 2N_i > R_{\mathrm{SE}}. \end{cases} \tag{B4}$$

Comparing (B4) with (A3) we have

$$\begin{cases} A_n = 0, B_n = -\frac{1}{2\varepsilon_0}(-1)^n 2^n N_i^n & \text{if } 2N_i < R_{\text{SE}} \\ A_n = -\frac{1}{2\varepsilon_0}\frac{(-1)^n}{2^{n+1}N_i^{n+1}}, B_n = 0 & \text{if } 2N_i > R_{\text{SE}}. \end{cases} \tag{B5}$$

The position $\mathbf{r}_{\text{E}}$ can also be re-written as $(R_{\text{SE}}, \pi/2, 0)$ in spherical coordinates. Substituting (B5) into (A3) then gives

$$U(\mathbf{r}_{\text{E}}) = \begin{cases} -\frac{1}{2\varepsilon_0}\sum_{n=0}^{\infty}\frac{(-1)^n 2^n N_i^n}{R_{\text{SE}}^{n+1}}P_n(0) & \text{if } 2N_i < R_{\text{SE}} \\ -\frac{1}{2\varepsilon_0}\sum_{n=0}^{\infty}\frac{(-1)^n R_{\text{SE}}^n}{2^{n+1}N_i^{n+1}}P_n(0) & \text{if } 2N_i > R_{\text{SE}}. \end{cases} \tag{B6}$$

Since the Legendre polynomials can be expressed in differential form, namely

$$P_n(x) = \frac{1}{2^n n!}\frac{\mathrm{d}^n}{\mathrm{d}x^n}\left[\left(x^2-1\right)^n\right],$$

we have that

$$P_n(0) = \begin{cases} \frac{(-1)^m}{2^{2m}}\frac{(2m)!}{(m!)^2} & \text{for} \quad n = 2m \\ 0 & \text{for} \quad n = 2m+1. \end{cases} \tag{B7}$$

From Taylor series we have

$$\frac{1}{\sqrt{1+x}} = \sum_{m=0}^{\infty}\frac{(-1)^m}{2^{2m}}\frac{(2m)!}{(m!)^2}x^m \tag{B8}$$

when $|x| < 1$. Substituting (B7) and (B8) into (B6) gives

$$U(\mathbf{r}_{\text{E}}) = -\frac{1}{2\varepsilon_0\sqrt{R_{\text{SE}}^2 + 4N_i^2}}. \tag{B9}$$

One can find (B1) equating the right hand sides of (B9) with (A12). □